

# Performance of the MICE diagnostic systems

5

A.N. Other et al.

## Abstract

This paper will describe:

- The detectors as we have it installed in the MICE Hall at November 2017
- The performances of the detectors and the PID
- The absorbers model(s) and their validation
- The track matching
- The detector alignment

10

Reference to the published papers. Target: JINST volume.

Table 1: Status of the paper

Contribution	Plots	Text
TOF	Second version	First version
Cherenkov	First version	First version
KL	First version	First version
EMR	All in v3.2.0	First version
Tracker	First version	First version
PID	First part	First part
Track matching	First version	First version
Detector alignment	All in v3.2.0	First version
Absorber model	First version	First version

## Contents

15	<b>1 Introduction</b>	2
	<b>2 Time-of-Flight Detectors</b>	2
	2.1 Introduction . . . . .	2
	2.2 Calibration Method . . . . .	4
	2.3 Reconstruction . . . . .	7
20	2.4 Performance . . . . .	8
	<b>3 Cherenkov Detectors</b>	9
	3.1 Introduction . . . . .	9
	3.2 Performance . . . . .	11
	<b>4 KLOE-Light Calorimeter</b>	13
25	4.1 Introduction . . . . .	13
	4.2 Performance . . . . .	13

<b>5</b>	<b>Electron Muon Ranger</b>	<b>17</b>
30	5.1 Introduction . . . . .	17
	5.2 Performance . . . . .	18
	<b>6</b> Trackers	<b>25</b>
	6.1 Introduction . . . . .	25
	6.2 Tracker Performance and Reconstruction . . . . .	26
	6.3 Tracker Efficiency Evolution . . . . .	30
35	<b>7</b> Particle ID	<b>30</b>
	7.1 Algorithm . . . . .	31
	7.2 Performance of the PID . . . . .	32
	<b>8</b> Global Track Matching reconstruction	<b>32</b>
	<b>9</b> Beam-based detector alignment	<b>39</b>
40	9.1 Introduction . . . . .	40
	9.2 Analysis method . . . . .	41
	9.3 Alignment of a data sample . . . . .	42
	9.4 Propagation . . . . .	43
45	<b>10</b> Liquid Hydrogen absorber	<b>45</b>
	10.1 Introduction . . . . .	45
	10.2 Systematic studies . . . . .	46
	10.3 Validation of the absorber model in MAUS . . . . .	50
	<b>11</b> Conclusions	<b>52</b>

## 1 Introduction

To include:

- 50   • Motivation
- Outline of the experiment

## 2 Time-of-Flight Detectors

### 2.1 Introduction

Three time-of-flight detectors (TOF0, TOF1, TOF2) were built and installed at RAL in 2008 and 2009 to measure the position and the time of crossing particles. TOF0 and TOF1 [1], [2], [3] were placed upstream of the cooling channel, and TOF2 [4] was downstream of the channel, mounted in front of the KL, as shown in Fig. 1. The time of flight between two TOF stations provides particle identification information and can also be used for momentum measurement. TOF1 served most of the time also as an experimental trigger. They operated smoothly during the so-called Step I and Step IV [5], [6] running periods of the MICE experiment and 60 were essential for all the measurements done.

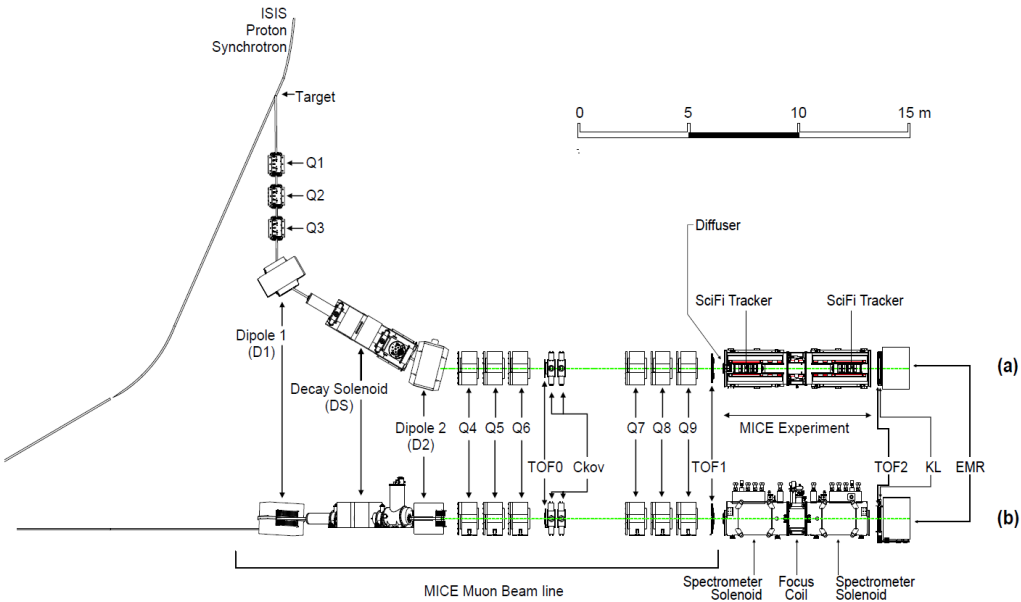


Figure 1: MICE experiment in the Step IV configuration, showing the full beam line and cooling channel elements with all the detectors.

The good performances of the TOF detectors, over an extended period of time, enabled the MICE experiment to characterize fully its muon beams during Step I data-taking, by measuring their emittance [7] and assessing their pion contamination [8].

Each TOF station was made of two planes of fast 1" thick scintillator bars oriented along X and Y directions, respectively. The bars were made of BC404 plastic scintillator<sup>1</sup>. A simple fishtail light-guide was used to attach each end of a bar to R4998 Hamamatsu fast photomultiplier tubes<sup>2</sup>. R4998 PMTs were delivered by Hamamatsu in assemblies (H6533MOD) that included the PMT tube, the voltage divider chain and a 1 mm thick  $\mu$ -metal shield, extending 30 mm beyond the photocathode surface. To increase the count rate stability active dividers were used, instead of conventional resistive ones. Illustration of TOF1 station is shown in Figure 2 together with an exploded view of a slab.

The stations TOF0, TOF1, and TOF2 had active areas of  $40 \times 40 \text{ cm}^2$ ,  $42 \times 42 \text{ cm}^2$ , and  $60 \times 60 \text{ cm}^2$  respectively. Each of the planes in TOF0 station had 10 4-cm wide scintillator slabs. Stations TOF1 and TOF2 used 7 and 10 in each plane, respectively. The PMTs are connected to a 50% – 50% passive splitter using  $\sim 34 \text{ m}$  long RG213 signal cable. One half of the signal is fed to the leading-edge CAMAC Lecroy 4115 discriminator followed by CAEN V1290 TDC for time measurements. Second half of the signal goes to CAEN V1724 FADC for pulse-height measurements. Pulse height measurement is instrumental for time-walk corrections. Each station issued a local readout trigger if signals in both PMTs attached to a slab crossed a specific threshold. All three stations were read out when TOF1 station issued a local trigger. This readout trigger was also used for the rest of the MICE detector systems.

All stations were exposed to residual magnetic fields: TOF0 station was placed in a relatively low residual field produced by the last quadrupole magnet of the beam line, while the other two TOF stations were exposed to the stray fields of the cooling channel solenoids. A shielding structure was adopted covering all PMTs at each side of the stations. Fig. 3 shows photographs from the assembly of the TOF2 station at INFN MIB, taken

<sup>1</sup>Emission maximum at 408 nm, decay time 1.8 ns, attenuation length 160 cm

<sup>2</sup>one-inch linear focused PMTs with 10 stages, typical gain  $G \sim 5.7 \times 10^6$  at -2250 V and  $B=0$  T, rise time 0.7 ns, transit time spread (TTS)  $\sim 160$  ps

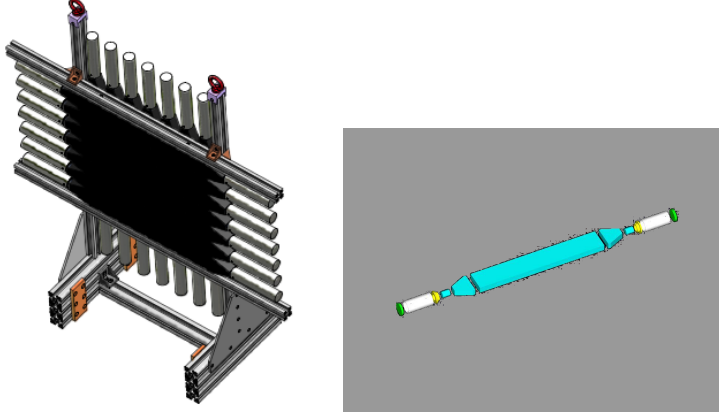


Figure 2: TOF design [9] and slab components [2].



Figure 3: Assembly of TOF2 at INFN MIB mechanics workshop. Left to right: from the bare magnetic shielding to the fully assembled counters of one plane.

from [4].

85 The purpose of the TOF system is to effectively discriminate particle species based on time-of-flight measurement. The main components in the MICE beam are muons, pions, and electrons. The time resolution needs to be sufficiently good to effectively discriminate between these types. At 240 MeV/c, the time-of-flight difference between muon and pion is about 1.3 ns between TOF0 and TOF1 stations. With 200 ps resolution, one reaches near 100% discrimination efficiency.

## 90 2.2 Calibration Method

Measurement of time traversal of a particle through a TOF station is influenced by several factors at the hardware level. When a particle crosses the plastic scintillator, there is a short delay in light production, with a characteristic decay time of 1.8 ns.

95 After generation, scintillation light propagates to the ends of each scintillator slab where it is detected by photomultiplier tubes. The light-travel time depends on the distance of the particle crossing from the PMT. The lengths of slabs in TOF0, TOF1, and TOF2 were 40 cm, 42 cm, and 60 cm, respectively. This translates to about 3 ns, 3.1 ns, and 4.4 ns, respectively, as the effective light propagation speed in the scintillator was found to be approximately 13.5 cm/ns.

More delay was introduced by the transit time of each PMT and of the cable that led the signal to the 100 readout electronics. These times were unique for each individual PMT channel and needed to be determined in dedicated measurements.

The times of each signal of a PMT were measured as times of signal threshold crossings in a simple linear discriminator. This introduced bias in the measured time dependent on the total charge of the signal, effect

referred to as time-walk.

105 Signal times of each channel were recorded in TDC boards. Readout of the whole system was triggered by having a signal in TOF1 station. The readout trigger signal is distributed to all TDC boards and is used as a reference time. Which PMT channel's threshold crossing caused the readout was depending on where the particle crossed through the TOF1 station. As a consequence, the reference time had a bias dependent on the position of TOF1 crossing, an effect referred to here as trigger delay.

110 The final time measurement in each station was determined as an average of the times of individual channels. This way, different distance from the point of crossing to each side of the scintillator slabs does not matter anymore, because the average of the times of the 2 PMTs does not depend on it.

115 Corrections which need to be made to the measured times are then the time-walk correction, the PMT channel specific delay time  $T_0$ , and a correction for the reference trigger time delay.

120 Details of the calibration method are described in [10].

## 2.2.1 Time-walk Correction

First correction to the measured time of each channel is time-walk correction. It was considered to be a static property of each channel. The same correction was used for all runs. The correction was determined by looking at time difference between two selected channels of slabs from different planes.

125 Let  $T^{ijk}$  denote a TDC measured time in PMT  $k$  of a slab  $j$  in a plane  $i$ . Similarly, let  $ADC^{ijk}$  be the measured pulse height in that PMT channel. Then time-walk of PMT  $k$  in slab  $j$  of plane 0 was determined from the 2D distribution of  $T^{14k'} - T^{0jk}$  vs.  $ADC^{0jk}$ . The reference channel was chosen from slab in the middle of the other plane (slab 4 in this example). PMT with higher mean ADC count was selected.

130 A special pre-correction was first determined for reference slabs, middle slabs in each plane. Only events where particle crossed the pixel corresponding to their crossing were considered. The pixel was in the centre of the station and was always well populated with particles crossing it. The ADC count in one of the slabs taken as a reference was limited to a 10% region around its mean. The TDC time of the slab was then little affected by the time walk.

The following function was fitted to the profile of the 2D data histogram:

$$f(ADC) = P_1 + \frac{P_2}{ADC - P_0} + \frac{P_3}{(ADC - P_0)^2}. \quad (1)$$

135 Where possible, parameter  $P_3$  was fixed to 0. For some PMTs such fit would not follow the measured trend and the additional parameter was added to the fit.

After the pre-correction of the reference slabs, time-walk of all the PMT channels was determined by looking at events in pixels corresponding to the crossing with the reference slab.

An example of time walk of a channel with respect to pre-corrected time in a reference slab is shown in Figure 4. The residual effect of time walk after the correction is also shown.

140 Figure 5 shows distributions of time differences between horizontal slab 4 and vertical slab 5 before and after the time-walk correction. The width of the distribution is significantly decreased. The mean of the distribution is not centered at 0 as differences in delays  $T_0$  were not accounted for, yet.

## 2.2.2 Trigger Delay Correction

Station TOF1 was used to trigger the readout of the whole system. Time of it's trigger signal was used as a reference signal for time measurements of all 3 stations. Depending on position where a particle was crossing the TOF1 station, this trigger signal will have different delays. The delay of each pixel was measured relative

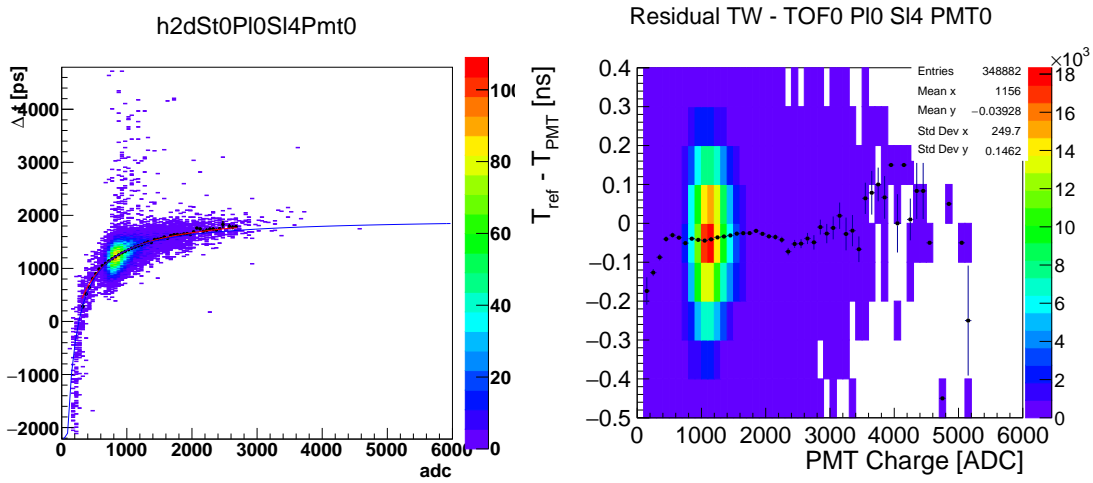


Figure 4: Time walk (left) in PMT 0 of slab 4 in plane 0 (horizontal) of station TOF0. The 2D histogram (coloured scale) is overlaid with its profile and with the fit function described in Eq. 1. Residual time walk (right) after the correction was applied.

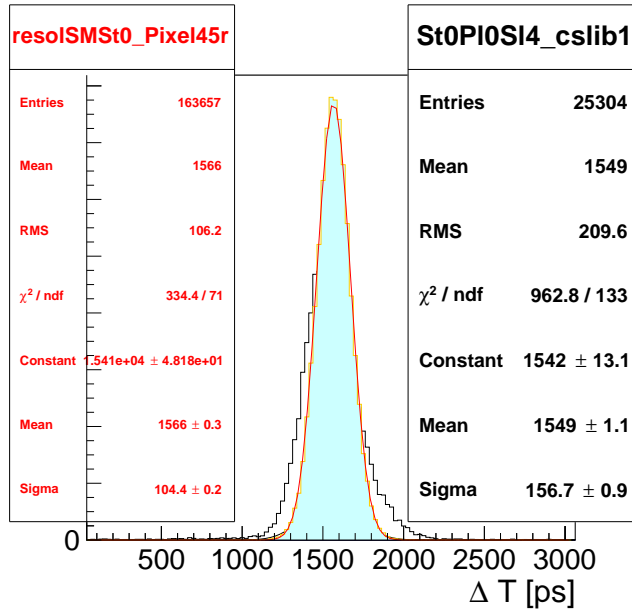


Figure 5: Distribution of time differences  $\Delta T$  between horizontal slab 4 and vertical slab 5 in station TOF0. Distribution before and after the time-walk correction are overlaid.

to the central pixel of TOF1 station. It was assumed that the source of the delay for individual pixel did not change from event to event. Although in reality this was not the case for most of the pixels, it was a good enough approximation.

Determination of the trigger delays for each pixel was as follows: Times of each PMT were corrected for time walk first. Trigger delay of the central pixel, defined as a crossing of station's 2 reference slabs, was set to 0. Trigger delays of the rest of the pixels in the reference slabs were calculated from differences of mean times of each PMT. For example, for pixels  $i$  of the horizontal reference slab refx, the trigger delay time  $T_{\text{refx},i}^{\text{trig}}$  is given by:

$$T_{\text{refx},i}^{\text{trig}} = \frac{1}{2} \sum_{\text{PMT}} \left\langle t_{\text{refx},i}^{\text{PMT,refx}} \right\rangle - \left\langle t_{\text{refx,refy}}^{\text{PMT,refx}} \right\rangle, \quad (2)$$

where  $t_{i,j}^{\text{PMT},i}$  is the time in PMT of slab  $i$  for events where particle crossed pixel  $i, j$ . The delays are averaged over both PMTs of the slab. Pixel denoted refx,refy is the central reference pixel of the TOF1 station.

For the rest of the pixels, not defined by the reference slabs, the trigger delay times were determined as a delay with respect to the pixels on the reference slabs. Delays of those reference pixels were then added:

$$T_{i,j}^{\text{trig}} = \frac{1}{4} \sum_{\text{PMT}} \left( \left\langle t_{i,j}^{\text{PMT},i} \right\rangle - \left\langle t_{i,\text{refy}}^{\text{PMT},i} \right\rangle + \left\langle t_{i,j}^{\text{PMT},j} \right\rangle - \left\langle t_{\text{refy},j}^{\text{PMT},j} \right\rangle \right) + \frac{1}{2} \left( T_{i,\text{refy}}^{\text{trig}} + T_{\text{refx},j}^{\text{trig}} \right) \quad (3)$$

### 2.2.3 $T_0$ Correction

Times in each channel were also corrected for the channel specific delays caused by each PMT and by the cable lengths. The correction was determined from times measured of particles crossing through the middle pixel of each slab. The times were corrected for the time walk and for TOF0 and TOF2 stations also for the trigger signal delay. The correction for TOF1, the readout triggering station, were set such that the mean of the time distribution was at 0.

Times in TOF0 and TOF2 stations reflected the time of flight of individual particles to and from TOF1. Distribution of the times in those stations show 3-peaked structure, where the most isolated peak at lowest time-of-flight corresponds to the electrons. They travel at the speed of light and their time of flight was calculated from distances from TOF1 station. Corrections for each channel were determined such that the electron peak was located at the predicted time of flight.

Figure 6 shows position of the electron peak as measured by TOF0 station in one run with beam at nominal 140 MeV/c. Uncorrected raw times are compared to fully corrected time. Corrected-time distribution shows better electron peak separation and it also places it to the correct position relative to TOF1.

Due to the presence of focusing fields in the beam-line section between TOF0 and TOF1 stations, particles did not travel in a straight line in that section. Deviation from a straight line was dependent on the initial direction and momentum of the particles entering the section. The effect was estimated [9] in simulations to be of an order of  $\sim 30$  ps. This effect caused a small bias in the calibrations.

## 2.3 Reconstruction

Particle crossing a TOF station must have crossed 2 orthogonal slabs in the stations 2 planes. The time and approximate position of particle crossing a TOF station was reconstructed from the PMT signals in the two slabs. Each slab with at least one recorded signal in each of the 2 attached PMTs was considered as being crossed by a particle. Times of these recorded signals were corrected for time-walk, readout trigger signal delay, and the channel specific delay. Time of crossing of the slab was then taken as the average of the 2 corrected PMT times.

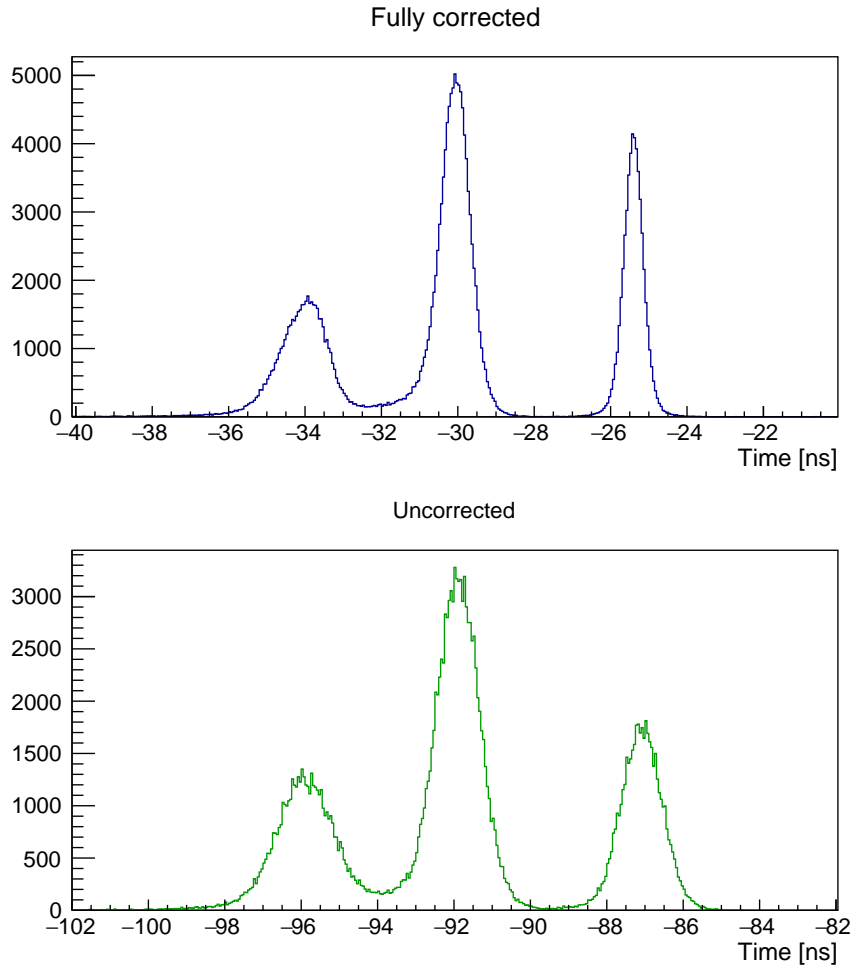


Figure 6: Example of time distribution of events in TOF0. Times before any corrections are compared to to times with all corrections applied.

The 2 slabs hit by a particle defined a pixel of area given by the width of the slabs. Sometimes, there were  
 180 more slabs in each plane with signals. Matching of 2 slabs being crossed by a particle was done based on their measured signal time. They were matched if the times were within a 4-ns window. The time of the particle crossing was determined as the average of times of the 2 matched slabs.

In order to be able to correct for the trigger signal delay, the pixel through which the particle crossed TOF1 needed to be determined. All possible combinations of 2 slabs from 2 different planes were tested. The times  
 185 of the recorded PMT signals were corrected under the hypothesis that correct slabs were matched. The pixel of the crossing particle was identified if the time difference of the 2 slabs was shorter than 4 ns.

## 2.4 Performance

Resolution of time-of-flight measurement is given by time resolution of each station. The time of a station particle crossing is determined from the average of times of the two slabs. The resolution of the average is a  
 190 half of the spread of their difference. Therefore, looking at slab  $\Delta T$  allows determination of the time-of-flight resolution.

Due to the errors in calibrations, especially in the underpopulated peripheral pixels, the slab  $\Delta T$  distributions have slight offsets from 0. Also, the spread of the distributions varies from pixel to pixel. The offsets and the

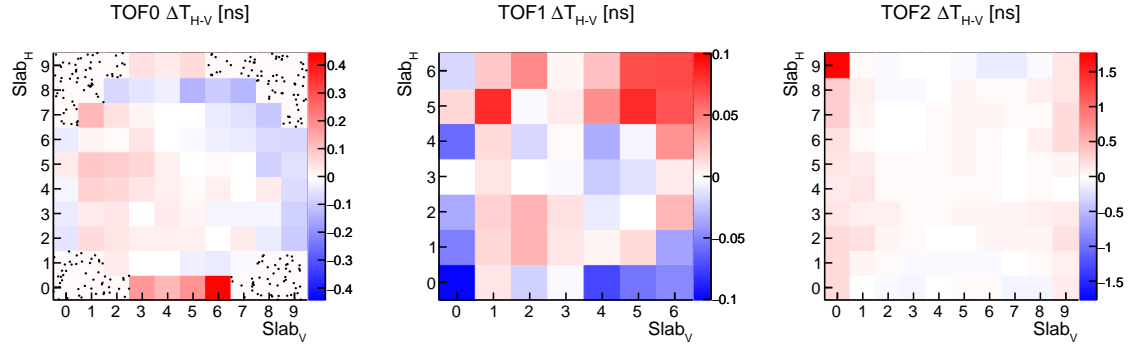


Figure 7: Offsets in slab  $\Delta T$  for individual pixels for all 3 stations.

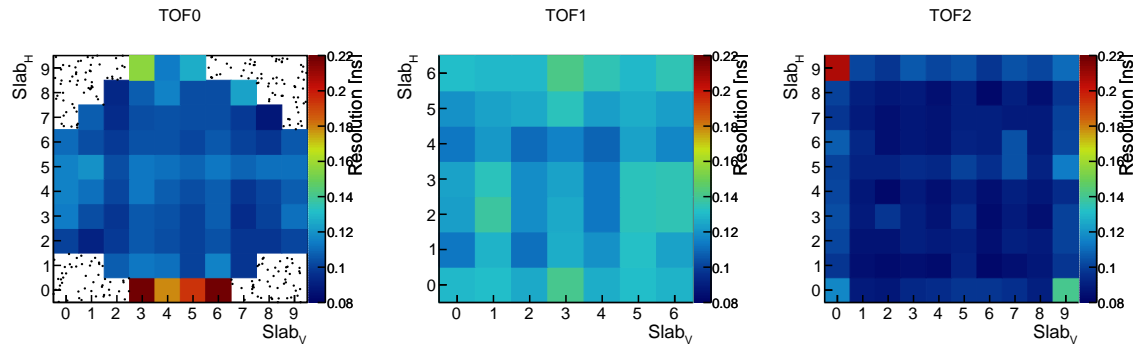


Figure 8: Spread in the slab  $\Delta T$  distributions of each pixel.

spreads of the slab  $\Delta T$  distributions for individual pixels are shown in Figures 7 and 8, respectively.

Overall performance can be inferred from the combined slab  $\Delta T$  distributions. The plots in Figure 9 show that they all centre approximately at 0 ns and they exhibit very similar resolutions, with TOF1 having the largest spread.

The reconstruction of a pixel by matching of 2 slabs from different planes of each station is dependent on the slab  $\Delta T$ . The 4 ns time window for the matching was chosen to cover the errors of the calibrations. Yet, there were times when there were signals in slabs in each plane of a station, but they were never matched. These events were mostly results of multiple particles passing through the station and causing signal in one plane only. They would never be matched in time as they arrived within the beam bunch time stretch of about 1  $\mu$ s. Figure 10 shows fractions of events where there were signals in two perpendicular slabs and they were time-matched. One can see lower efficiency/fraction in the peripheral pixels which is associated with the larger fraction of multiple particle crossings with giving signal in one slab only.

### 3 Cherenkov Detectors

#### 3.1 Introduction

The MICE Cherenkov threshold detectors, measuring velocity, are primarily designed to provide  $\pi$ - $\mu$  separation in the higher momentum ranges, where TOF peaks separation is not sufficient for conclusive particle identification.

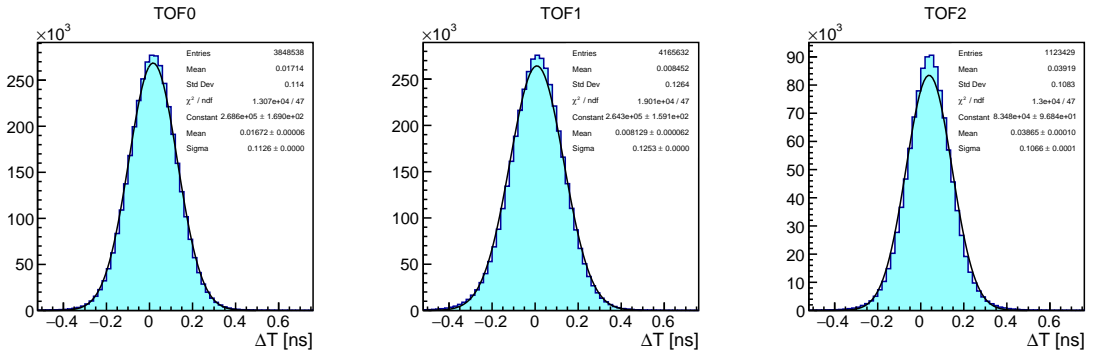


Figure 9: Overall slab  $\Delta T$  distributions. Total width of the distribution is due to the resolution of individual pixels and due to the offsets in their  $\Delta T$  distributions.

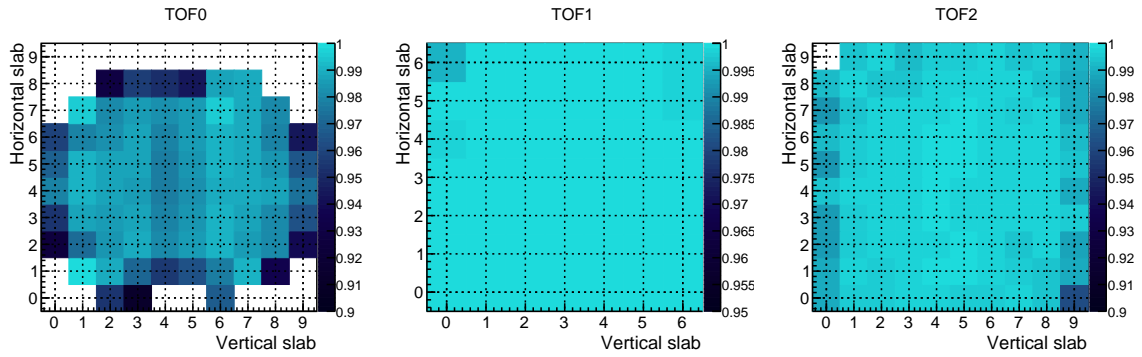


Figure 10: Efficiency of space point creation if there were hits in two transverse slabs.

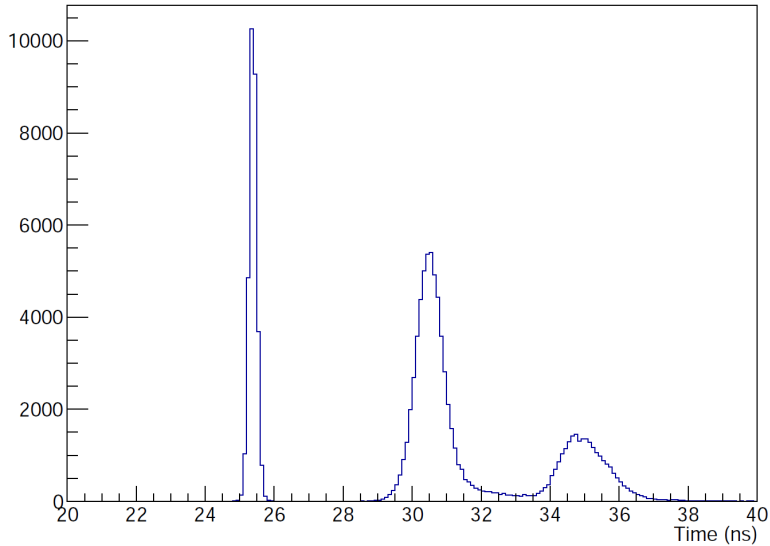


Figure 11: Time of flight between TOF0 and TOF1 for a “pion” beam. From the left: the well separated electron, muon and pion peaks.

In order to provide separation over a large range of momenta, two high density silica aerogel Cherenkov

detectors (CkovA and CkovB) with refractive indices  $n=1.07$  and  $n=1.12$  are used. Light is collected in each counter by four 9354KB eight-inch UV-enhanced phototubes and recorded by CAEN V1731 FADCs (500 MS/s). The two detectors are placed directly one after another in the beamline, located just after the first TOF counter. In Fig. 12 an exploded view of one detector is shown.

Their respective thresholds provide different responses in four distinct momentum ranges, i.e. in the 200 MeV/c beams, pions are below the threshold which would fire the detector for both CkovA and CkovB whereas muons are above only for CkovB, while for the 240 MeV/c beams, pions are above the threshold for CkovB while muons are above for both CkovA and CkovB. Using this information algorithms can be written that produce likelihood distributions of particle type. Below the CkovB muon threshold of about 217.9 MeV/c, where there is no separation, the TOFs provide good separation, whereas the momentum range above the CkovA pion threshold 367.9 MeV/c is outside of the MICE running parameters [11]. For unambiguous identification of particle species the Cherenkov detectors would need a momentum measurement from the MICE Tracker.

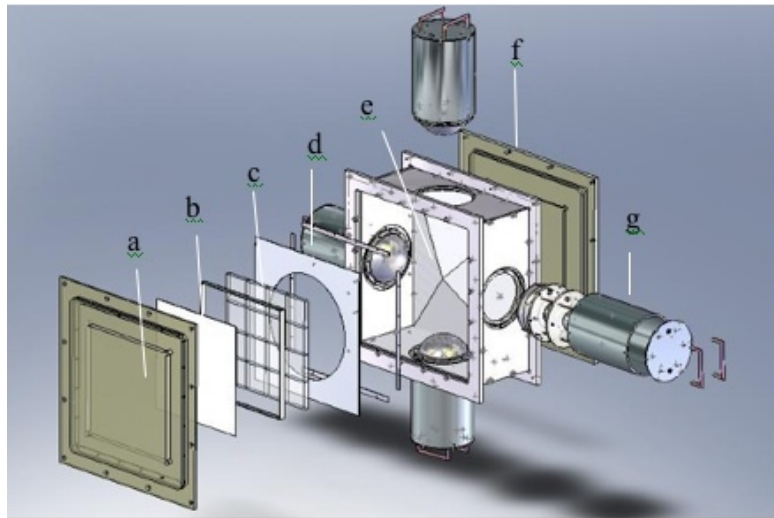


Figure 12: MICE aerogel Cherenkov counter blowup: a) entrance window, b) mirror, c) aerogel mosaic, d) acetate window, e) GORE reflector panel, f) exit window and g) eight-inch PMT in iron shield.

### 3.2 Performance

The data sets used to evaluate the Cherenkov detectors are summarized in Table 2. A wide range of settings (including alignment runs) has been used in order to cover the full spectra of particles that could have been measured by the detectors.

The asymptotic light yield (for  $\beta=v/c=1$ ) in each counter has been measured using the electron peaks, giving  $16 \pm 1$  photoelectrons (NPE) in CkovA and  $19 \pm 1$  in CkovB.

The photoelectrons yields versus momentum for muons and pions in CkovA and CkovB are displayed in Fig. 13, using the time of flight between TOF0 and TOF1 to select the species and estimate the momenta. The distributions of NPEs as a function of the momentum P have been fitted with the function

$$NPE(P) = NPE_0 + NPE_{\beta=1} \left( 1 - \left( \frac{P_0}{P} \right)^2 \right) \quad (4)$$

where  $NPE_0$  is the number of background photoelectrons,  $NPE_{\beta=1}$  is the asymptotic light yield and  $P_0$  is the momentum threshold.

Run ID	Date	Nominal momentum [MeV/c]	Spills	Triggers
10488	12/12/2017	140	3777	300269
10496	12/12/2017	170	4180	371037
10391	03/12/2017	200	2146	240033
10419	04/12/2017	240	2932	328062
10304	29/11/2017	300	2502	305363
10221	23/11/2016	300	4493	560119
10519	15/12/2017	400	4316	506384

Table 2: Summary of the data sets used to visualize the activation curve of the MICE Cherenkov detectors.

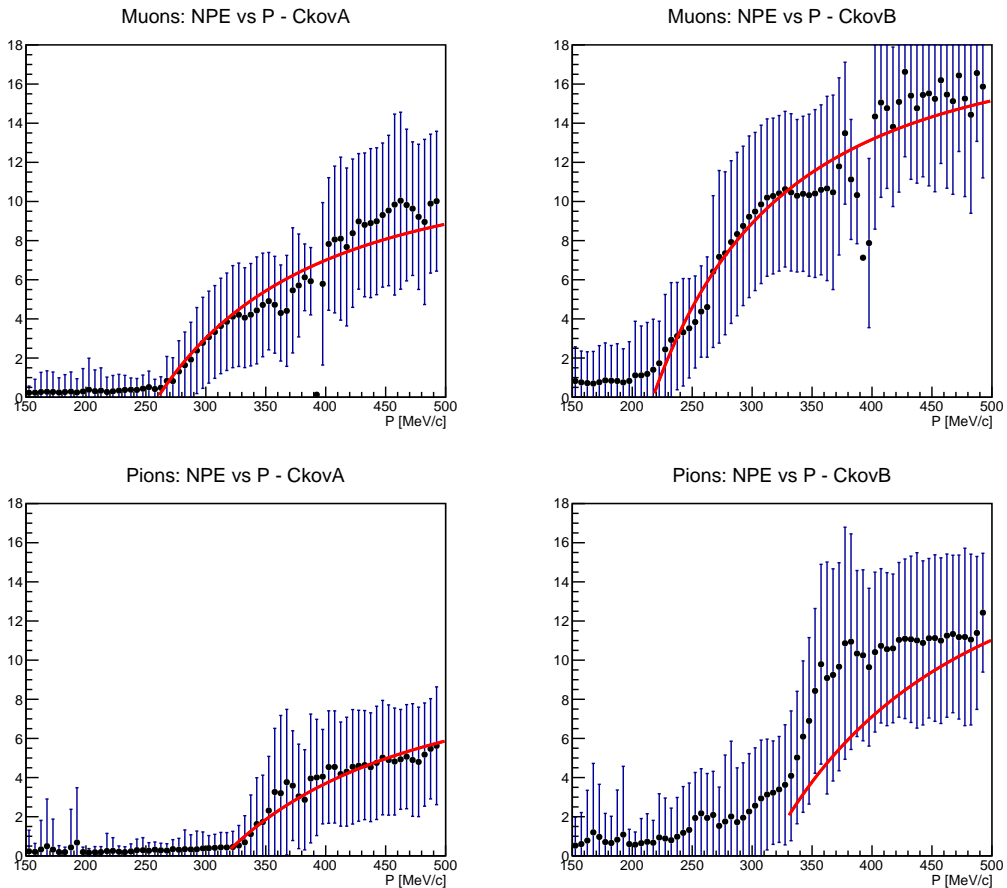


Figure 13: Photoelectron yields versus momentum for muons and pions in CkovA and CkovB with the superimposed fitted activation functions. The error bars correspond to the standard deviation for each momentum bin.

235 The observed muon thresholds are  $267.3 \pm 18.1$  and  $219.4 \pm 14.5$  MeV/c, while for pions are  $332.2 \pm 38.4$  MeV/c and  $295.9 \pm 95.9$  MeV/c, respectively in CkovA and CkovB. The  $NPE_{\beta=1}$  values are generally lower than the values predicted as in a previous analysis [11] done with Step I data: this is mostly due to TOF0 acting as a pre-shower radiator.

In Fig. 14 is shown the typical photoelectron spectra for muons and pions well above the threshold. The 240 expected Poisson-like distribution receives tails from the electromagnetic showers and from secondary electrons

coming from interactions in TOF0 and in the aerogel itself.

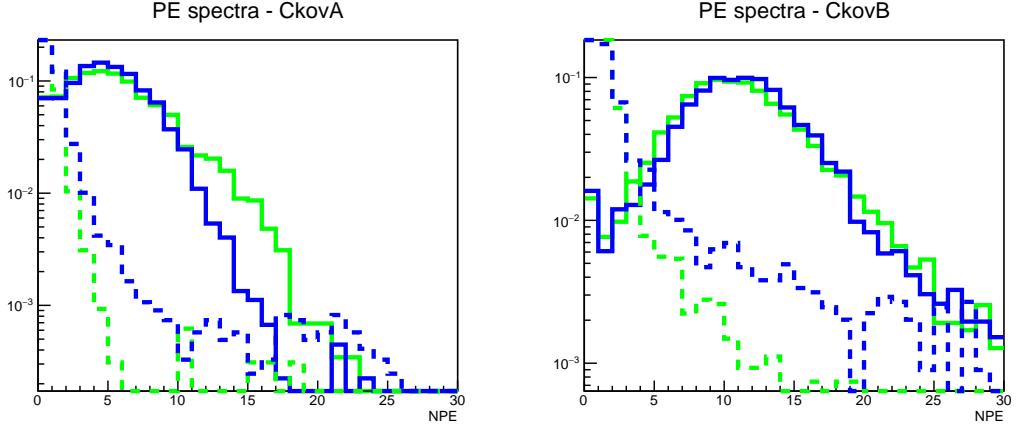


Figure 14: Photoelectron spectra in CkovA (left) and CkovB (right) for muons (green) and pions (blue) above (continuous line) and below (dashed line) the threshold. The distributions are normalised.

## 4 KLOE-Light Calorimeter

### 4.1 Introduction

The KLOE-Light (KL) pre-shower sampling calorimeter is composed of extruded lead foils in which scintillating fibres are placed in volume ratio scintillator:lead  $\sim 2:1$ , “lighter” than the one of the KLOE experiment calorimeter (1:1).

The fibres are 1 mm diameter BICRON BCF-12, scintillating in the blue, 1.35 mm distant from each other within a layer. The distance between two layers is 0.98 mm, one layer being shifted by half the fibre pitch with respect to the next. Scintillation light is guided from each slab into a total of six PMTs (three on each side). Iron shields are fitted to each photomultiplier to mitigate against large stray magnetic fields from the cooling channel (see Fig. 15). The signal from each PMT is sent to a shaping amplifier (SA) module, which shapes and stretches the signal in time in order to match the sampling rate of the flash ADCs (Fig. 16 shows the design of a single slab). A total of 7 slabs forms the whole detector, which has an active volume of  $93\text{ cm} \times 93\text{ cm} \times 4\text{ cm}$ .

With its 2.5 radiation lengths the KL is used to distinguish muons from decay electrons providing energy deposition and timing information and to act as pre-shower in front of the EMR. The detector has been used to estimate the level of pion contamination within the MICE muon beams to be around 1% [8].

### 4.2 Performance

The study of KL response to different particle types at different momenta is based on particle identification obtained by time-of-flight detector, as shown in the example of Fig. 11, by applying proper cuts on the time-of-flight spectrum. The performance is presented for 140, 170, 200, 240 and 300 MeV/c momenta at the absorber position, and depending of species population for muons, pions and electrons. The results presented below are obtained from the straight tracks data (i.e. without magnetic fields in the trackers or focus coil) taken mainly in 2017. The KL response to muons, pions and electrons for all available momenta is presented in Fig. 17. It is

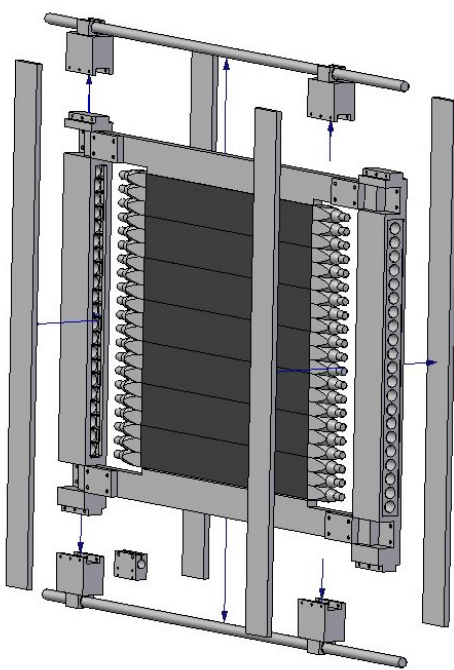


Figure 15: Magnetic shielding of KLOE-Light PMTs.

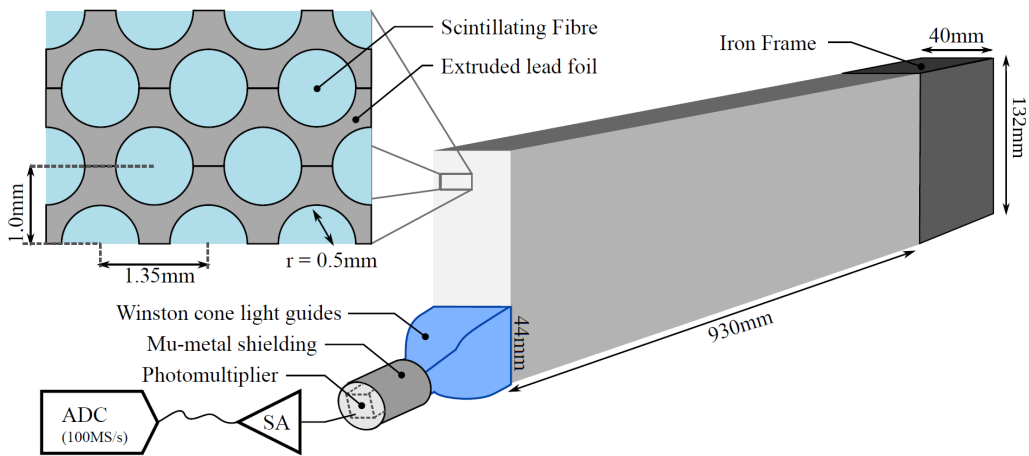


Figure 16: Single slab design of MICE KLOE-Light Calorimeter.

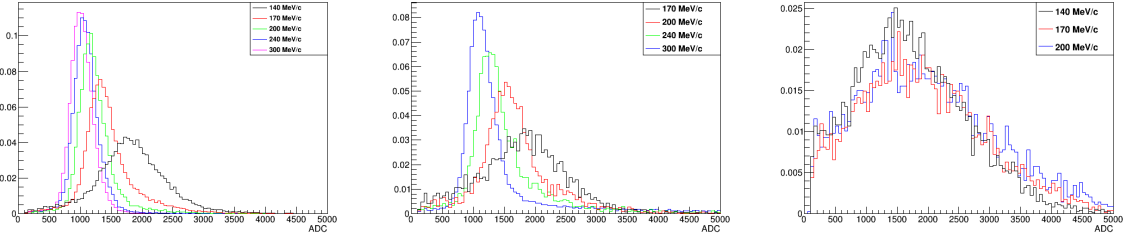


Figure 17: KL response to muons (left), pions (centre) and electrons (right) for several momenta. It is shown charge deposited by particles in KL in arbitrary units. All histograms are normalized to unity.

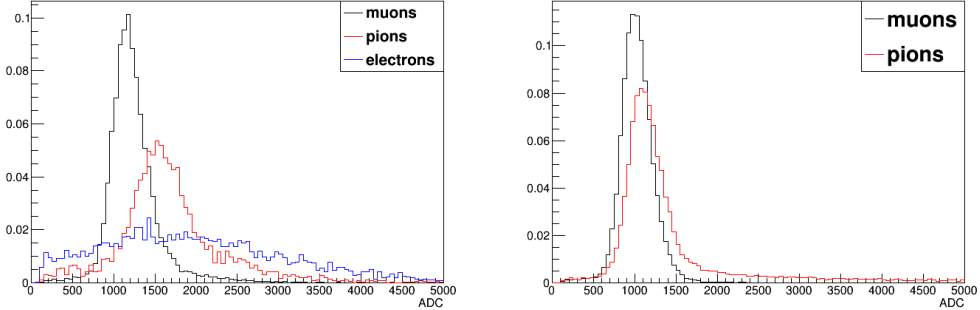


Figure 18: Comparison of energy deposition of muons, pions and electrons at 200 MeV/c (left) and of muons to pions at 300 MeV/c (right).

clear in the cases of muons and pions that they are below mip momenta since energy deposition decreases with momentum increasing<sup>3</sup>.

For comparison of energy deposition of muon, pions and electrons for fixed momentum Fig. 18 is presented. In the case of 300 MeV/c (Fig. 18, right), where muons and pions have almost the same maximum of distribution, the tail of pions is fatter than muon one. This is due to the fact that pions experience strong interaction as well. This pion behaviour has been used to estimate its contamination in muon sample.

The number of fired KL cells by a single muon, electron or pion is given in Fig. 19 for 240 MeV/c beam. For muons we expect one, in some cases two and almost never more fired cells depending on track inclination. Pions and electrons create avalanches in KL and electron ones is much wider than the pion ones as visible of number of KL cell hits. The same figure shows number of events when if there is a reconstructed TOF track, but no signal in KL above the threshold. This can be used to calculate efficiency of KL for the three species as a function of momentum. The results are presented in Table 3 and shows that efficiency for muon registration is close to 99%.

In Fig. 20 is shown simulation of KL response to 300 MeV/c muons and pions and the distributions are compared with data. The agreement between data and simulation is very good. The simulation is done via following steps:

- Smearing of produced photons in scintillator fibres. They obtain Poisson statistic so such is applied. In

<sup>3</sup>Actually the energy deposition is defined as the sum of ADC products from all cells in KL above a given threshold. The ADC product on the other hand is the product of left and right side of one slab divided by the sum of left and right side:  $ADC_{prod} = 2 \times ADC_{left} \times ADC_{right} / (ADC_{left} + ADC_{right})$ . The factor 2 is present for normalization. The product of two sides compensates the effect of attenuation.

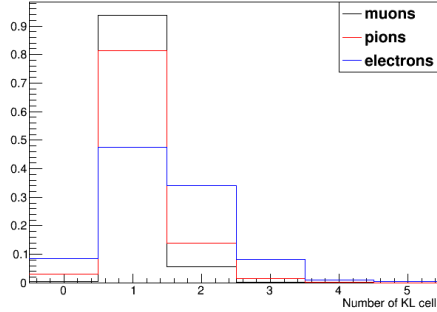


Figure 19: Particle multiplicity for 240 MeV/c, i.e. number of KL cells fired.

species	<b>140 MeV/c</b>	<b>170 MeV/c</b>	<b>200 MeV/c</b>	<b>240 MeV/c</b>	<b>300 MeV/c</b>
<b>electrons</b>	$0.95 \pm 0.02$	$0.95 \pm 0.01$	$0.94 \pm 0.03$	n/a	n/a
<b>muons</b>	$0.97 \pm 0.02$	$0.99 \pm 0.01$	$0.99 \pm 0.01$	$0.99 \pm 0.01$	$0.99 \pm 0.01$
<b>pions</b>	n/a	$0.89 \pm 0.03$	$0.95 \pm 0.03$	$0.97 \pm 0.03$	$0.98 \pm 0.01$

Table 3: Efficiency of KL for electrons, muons and pions as a function of particle momentum. The conditions required are existing of a TOF track and signal in KL above the threshold. The uncertainties are statistical.

principal one can replace it with Gaussian because the number of photons created is large enough for such an approximation.

- Photoelectrons created on photomultiplier photocathode also have Poisson statistics. It cannot be replaced here with normal distribution because the number of photoelectrons is small enough so such an approximation is illegal.
- Photomultiplier gain obtains also statistical properties but it is neither Poisson nor gauss. Nevertheless it turns out that for simplicity one can use Gaussian distribution with mean value equals to PMT gain and sigma of distribution equals to half of the gain. KL photomultipliers have gain  $\sim 2 \times 10^6$ , so their sigma is simply  $10^6$ .

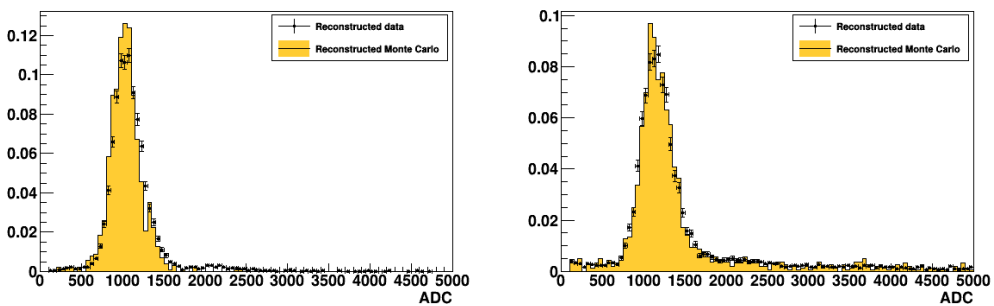


Figure 20: Comparison between data and Monte Carlo simulation of KL response to muons (left) and pions (right) at 300 MeV/c.

290 **5 Electron Muon Ranger**

## 5.1 Introduction

The Electron-Muon Ranger (EMR) is a fully-active scintillator detector [12]. It can be classified as a tracking-calorimeter as its granularity allows for track reconstruction. The EMR consists of extruded triangular scintillator bars arranged in planes. One plane contains 59 bars and covers an area of  $1.27 \text{ m}^2$ . Each even bar is rotated by 180 degrees with respect to the odd one. A cross-section of bars and their arrangement in a plane is shown in Fig. 21. This configuration does not leave dead area in the detector for particles crossing a plane with angles that do not exceed 45 degrees with respect to the beam axis. Each plane is rotated through 90 degrees with respect to the previous one, such that a pair of planes defines a horizontal and vertical ( $x, y$ ) interaction coordinate. The light, produced when a particle crosses a bar, is collected by a wave-length shifting (WLS) fibre glued inside the bar. At both ends, the WLS fibre is coupled to clear fibres that transport the light to a photomultiplier tube (PMT). Signals produced in a plane are read out collectively on one end by a single-anode PMT for an integrated charge measurement and separately on the other by a multi-anode PMTs for individual bar hit reconstruction. The full detector is composed of 24 X-Y modules for a total active volume of  $\sim 1 \text{ m}^3$ .

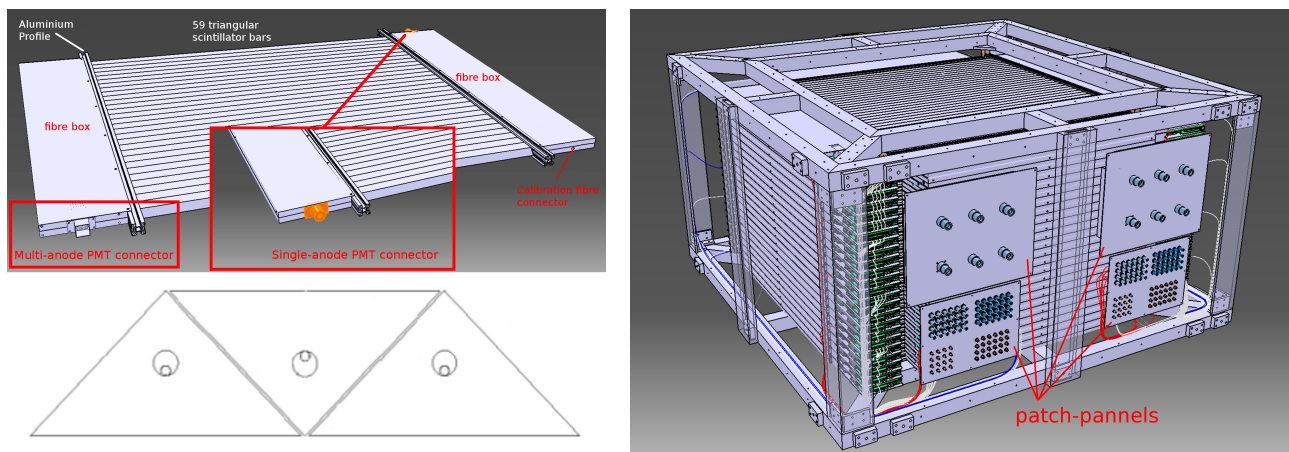


Figure 21: Drawing of one EMR plane (top left), cross section of 3 bars and their wavelength shifting fibres (bottom left) and drawing of the full detector and its supporting structure (right).

An array of analyses were conducted to characterize the hardware of the EMR and determine whether the detector performs to specifications [13]. The clear fibres coming from the bars were shown to transmit the desired amount of light, and only four dead channels were identified in the electronics. Two channels had indubitably been mismatched during assembly and the DAQ channel map was subsequently corrected. The level of crosstalk is within acceptable values for the type of multi-anode photomultiplier used with an average of  $0.20 \pm 0.03 \%$  probability of occurrence in adjacent channels and a mean amplitude equivalent to  $4.5 \pm 0.1 \%$  of the primary signal intensity. The efficiency of the signal acquisition, defined as the probability of recording a signal in a plane when a particle goes through it in beam conditions, reached  $99.73 \pm 0.02 \%$ .

The primary purpose of the EMR is to distinguish between muons and their decay products, identifying muons that have crossed the entire cooling channel. Muons and electrons exhibit distinct behaviours in the detector. A muon follows a single straight track before either stopping or exiting the scintillating volume, while electrons shower in the lead of the KL and create a broad cascade of secondary particles. Two main geometric variables, the plane density and the shower spread, are used to differentiate them. The detector is capable of identifying electrons with an efficiency of 98.6 %, providing a purity for the MICE beam that

exceeds 99.8 %. The EMR also proved to be a powerful tool for the reconstruction of muon momenta in the range 100–280 MeV/c [14].

## 320 5.2 Performance

The performance of the EMR detector is assessed at three levels of resolution with the data acquired during the 2017/02 and 2017/03 ISIS user cycles. The performance of the hardware itself is evaluated by analysing the characteristics of raw photomultiplier signals. The reconstruction efficiency is assessed by looking at higher level quantities. The performance of the detector as an electron tagging device is measured.

### 325 5.2.1 Hardware efficiencies

The data sets used to evaluate the detector hardware efficiencies are summarized in table 4. The MICE beam line is tuned to the highest attainable momentum to maximize the transmission to the EMR detector and increase the range of particles in the detector. In this configuration, the beam line produces pions and muons in comparable quantities, along with positrons. The particle species are identified by evaluating their time-of-flight between TOF1 and TOF2. The time-of-flight distribution for muons, pions and positrons is represented in figure 22. The muons and pions peaks are fitted with a sum of two Gaussians of the form

$$f_{\mu,\pi}(t_{12}) = \frac{A_{\mu,\pi}}{\sqrt{2\pi}\sigma_{\mu,\pi}} \exp\left[-\frac{(t_{12} - t_{\mu,\pi})^2}{2\sigma_{\mu,\pi}^2}\right]. \quad (5)$$

Only the particles with a time-of-flight between 28 and 28.75 ns, i.e. compatible with the muon hypothesis, are included in the analysis sample.

Run ID	Date	Type	Momentum	Spills	Triggers	EMR events
9619	19/09/2017	$\pi^+$	400 MeV/c	2289	265312	36775
9620	19/09/2017	$\pi^+$	400 MeV/c	5388	668026	107578
<b>Total</b>				7677	933338	144353

Table 4: Summary of the data sets used to measure the efficiency of the EMR in the 2017/02 ISIS user cycle.

A muon that makes it into the analysis sample has a momentum larger than 350 MeV/c right before TOF2. It is expected to cross both TOF2 and the KL without stopping and penetrate the EMR. In practice, the probability 330 of creating an EMR event, i.e. to produce hits in the detector is  $99.62 \pm 0.03 \%$ . The minor inefficiency may be attributed to pions in the muon sample that experience hadronic interactions in the KL. If hits are produced in the detector, space points are reconstructed  $98.56 \pm 0.06 \%$ . This inefficiency may be associated with muon that decay between TOF2 and the EMR and produce scarce hits in the detector.

To evaluate the efficiency of the scintillator planes and their readouts, only the muons which penetrate the entire detector are taken into account. If a signal is recorded in the most downstream plane, it is expected that at least a bar will be hit in each plane on its path and that a signal will be recorded in the single anode PMT. The left panel of figure 23 shows the MAPMT bar hit multiplicity for all the plane combined. It shows that in  $3.26 \pm 0.02 \%$  of cases, on average, a plane traversed by a muon will be not produce a signal in its MAPMT and that the most probable amount of bars hit is one. The right panel shows the distribution of charge recorded in the all the SAPMTs. A track is missed by an SAPMT  $1.88 \pm 0.01 \%$  of the time. This figure does not include SAPMT 26, turned off at the time of data taking.

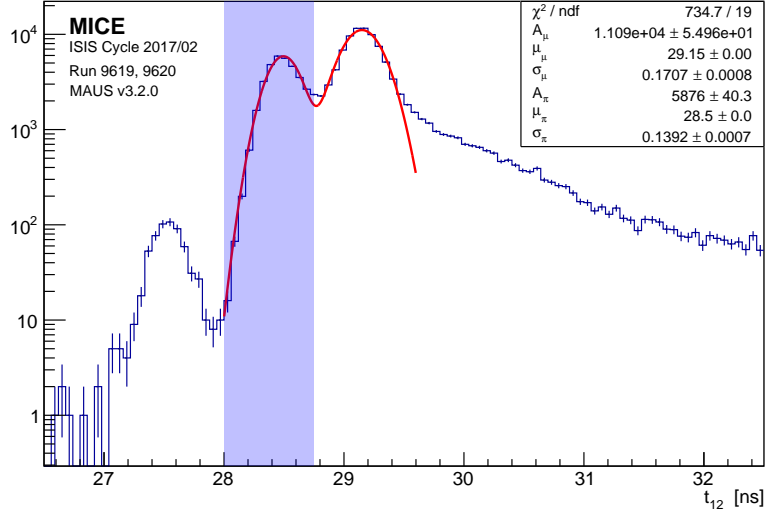


Figure 22: Time-of-flight of positrons, muons and pions for the  $400 \text{ MeV}/c$  pionic beam line used in the EMR efficiency analysis. The blue band represents the selected range.

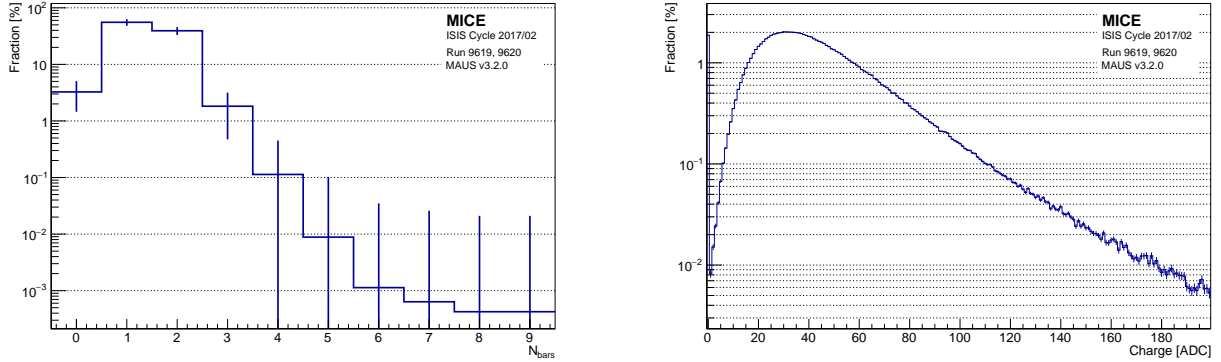


Figure 23: (Left) Global MAPMT bar multiplicity. (Right) Global SAPMT charge distribution.

Figure 24 shows the probability of recording a signal in individual MAPMTs and the SAPMTs for each of the 48 planes, given a muon that crosses the whole detector. The most inefficient PMTs miss the track  $\sim 10\%$  of the time. SAPMT 26 was experiencing issues during data taking and was turned off.

### 345 5.2.2 Electron rejection

The main purpose of the Electron-Muon Ranger is to tag and reject the muons that have decayed in flight inside the experimental apparatus. A broad range of beam line momentum settings, summarized in table 5, is used to characterize its muon selection efficiency. The particle species is characterized upstream of the detector by using the time-of-flight between TOF1 and TOF2. It exhibits three distinct peaks consisting of positrons, muons and pions, respectively, in order of increasing time-of-flight. The distributions of time-of-flight are shown for the data sets in range  $170\text{--}240 \text{ MeV}/c$  in figure 25. The limits of the peaks are fitted to each setting in order to separate the muons and positrons into two templates upstream of the EMR. Particles that fall above the upper

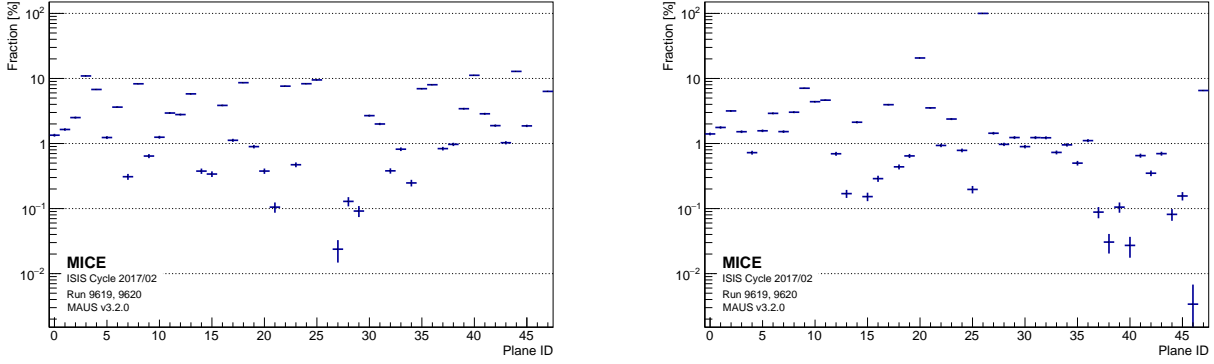


Figure 24: Probability of not producing a single bar hit in the MAPMT (left) and a zero charge in the SAPMT (right) in the 48 individual EMR planes.

limit of the muon peak are either pions or slow muons and are rejected from this analysis.

Run ID	Date	Type	Momentum	Spills	Triggers	EMR events
10268	26/11/2017	$\pi^+$	170 MeV/c	4418	328948	97452
10269	26/11/2017	$\pi^+$	170 MeV/c	3695	278330	82098
10262	25/11/2017	$\pi^+$	200 MeV/c	846	28103	8769
10266	25/11/2017	$\pi^+$	200 MeV/c	4365	148990	45448
10267	26/11/2017	$\pi^+$	200 MeV/c	4296	194207	53469
10275	26/11/2017	$\pi^+$	200 MeV/c	3547	126597	39114
10261	25/11/2017	$\pi^+$	240 MeV/c	4388	228337	66335
10264	25/11/2017	$\pi^+$	240 MeV/c	755	32322	10041
10265	25/11/2017	$\pi^+$	240 MeV/c	3336	134953	43129
10270	26/11/2017	$\pi^+$	240 MeV/c	222	17584	4030
10271	26/11/2017	$\pi^+$	240 MeV/c	66	5063	287
10272	26/11/2017	$\pi^+$	240 MeV/c	177	13538	1967
10273	26/11/2017	$\pi^+$	240 MeV/c	4339	232488	67350
10274	26/11/2017	$\pi^+$	240 MeV/c	738	38734	11123
<b>Total</b>			35188	1808194	530612	

Table 5: Summary of the data sets used to measure the efficiency of the EMR in the 2017/02 ISIS user cycle.

MICE is a single-particle experiment, i.e. the signals associated with a trigger originate from a single particle traversing the detector. The multi-anode readout of each detector plane provides an estimate of the position of the particle track in the  $xz$  or the  $yz$  projection, depending on the orientation of the scintillator bars. Figure 26 shows event displays of a muon and a positron, as observed inside the detector, in the  $xz$  and  $yz$  projections for particles in the 240 MeV/c beam line setting. The muon exhibits a clean straight track while the positron showers inside the lead of the KL and produces a disjointed and widespread signature. The particle identification variables used in the EMR are based on these distinct characteristics.

The first particle identification statistic is the plane density,  $\rho_p$ , defined as

$$\rho_p = \frac{N_p}{Z_p + 1}, \quad (6)$$

with  $N_p$  the number of planes hit and  $Z_p$  the number of the most downstream plane. A muon deposits energy in

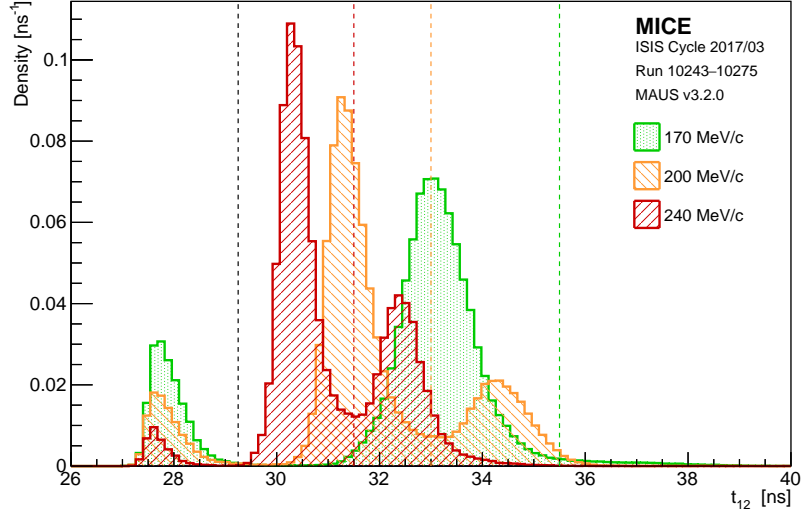


Figure 25: Time-of-flight distributions of the data sets in the range 170–240 MeV/c used in the EMR performance analysis. The dashed black line represents the upper bound of the positron peak and the coloured lines the upper bounds of the muon peaks in each setting.

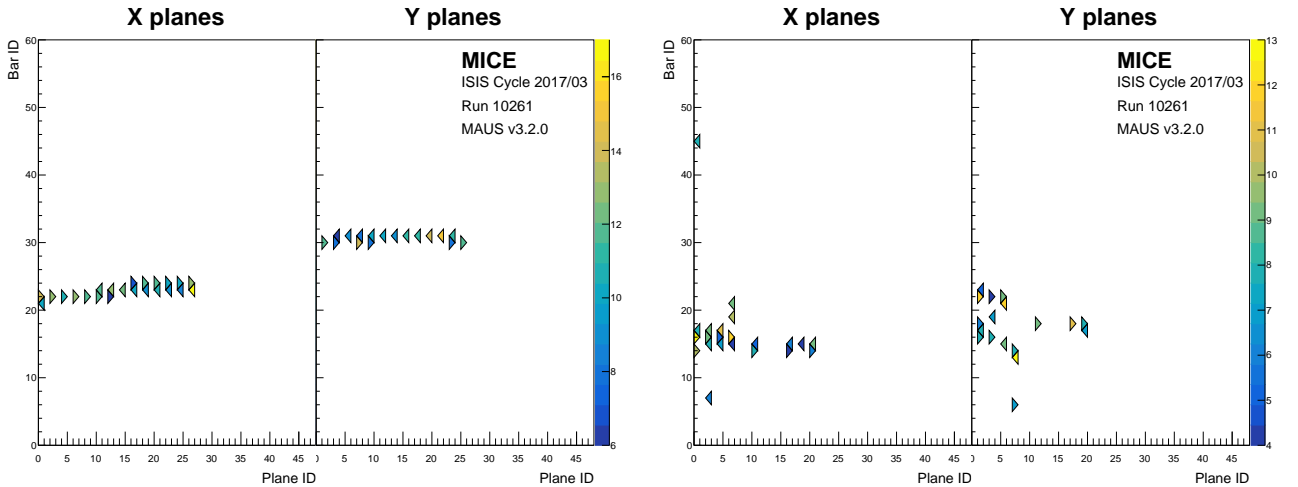


Figure 26: Event display of a muon (left) and a positron (right) from the 240 MeV/c beam line setting, in the  $xz$  and  $yz$  projections. The colour scale represents the time-over-threshold recorded in each channel, a digitized measurement of the energy deposition in the corresponding scintillator bar.

every plane it crosses until it stops, producing a plane density close or equal to one. A positron shower contains photons that may produce hits deep inside the fiducial volume without leaving a trace on their path, reducing the plane density. The left panel of figure 27 shows the distribution of plane density of the muon and positron templates. The two templates occupy significantly different regions of plane density, as expected.

The second variable is the normalised chi squared,  $\hat{\chi}^2$ , of the fitted straight track, i.e.

$$\hat{\chi}^2 = \frac{1}{N-4} \sum_{i=1}^N \frac{\text{res}_{x,i}^2 + \text{res}_{y,i}^2}{\sigma_x^2 + \sigma_y^2}, \quad (7)$$

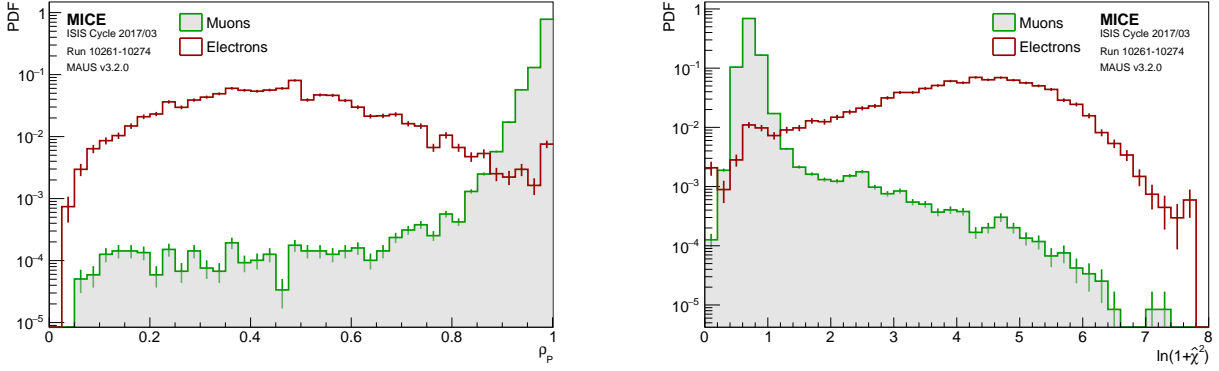


Figure 27: Plane density distribution,  $\rho_p$  (left), and normalised chi squared distribution,  $\hat{\chi}^2$  (right), of the muon and electron templates in the Electron-Muon Ranger.

with  $N$  the number of space points (one per bar hit),  $\text{res}_{q,i}$  the residual of the space point with respect to the track in the  $qz$  projection and  $\sigma_q$  the uncertainty on the space point in the  $qz$  projection,  $q = x, y$  [15]. The number of degrees of freedom is  $N - 4$ , as a three-dimensional straight track admits four parameters. This quantity represents the transversal spread of the particle's signature. A muon follows a single track and is expected to have a  $\hat{\chi}^2$  close to one, while an electron shower is expected to produce a larger value. The right panel of figure 27 shows the distribution of normalised chi squared of the muon and positron templates. The two templates occupy different regions of  $\hat{\chi}^2$  but overlap more than in the case of the plane density.

The two discriminating variables are combined to form a statistical test on the particle hypothesis. Given an unknown particle species, consider a set of cuts,  $(\rho_c, \hat{\chi}_c^2)$ , such that

$$\begin{aligned} \rho_p > \rho_c \cap \hat{\chi}^2 < \hat{\chi}_c^2 &\rightarrow \mu^+; \\ \rho_p < \rho_c \cup \hat{\chi}^2 > \hat{\chi}_c^2 &\rightarrow e^+. \end{aligned} \quad (8)$$

Dense and narrow events will be tagged as muons while non-continuous and wide electron showers will not.

The quality of a test statistic may be characterized in terms of the loss,  $\alpha$ , the fraction the muon sample that is rejected, and the contamination,  $\beta$ , the fraction of the electron sample that is selected. A test is optimal when the cost function,  $\Delta = \sqrt{\alpha^2 + \beta^2}$ , is minimized. Figure 28 shows the result of a scan over the parameter space. The left panel represents the cost,  $\Delta$ , as a function of the two parameters that define the test statistic. Each marker in the right panel represents the value of  $\alpha$  and  $\beta$  for the test values. The optimum choice of cuts yields a muon loss of 1.027 % and an electron contamination of 0.934 %.

The downstream tracker (TKD) allows for the reconstruction of each particle momentum before entering the EMR. To assess the influence of momentum on contamination and loss, their values are calculated for 10 MeV/c bins in the range 100–300 MeV/c. The test statistic performed in each bin is based on the optimal set of cuts optimized for the whole sample, i.e.  $\rho^* = 86.131\%$  and  $\hat{\chi}^{2*} = 14.229$ . Figure 29 shows the loss,  $\alpha$ , and the contamination,  $\beta$ , as a function the TKD momentum. It shows that, at low momentum, the apparent muon loss increases. This is due to an increase in decay probability between TOF2 and the EMR and an decrease in the amount of muons that cross the KL to reach the EMR.

### 5.2.3 Muon track momentum

The tracking capabilities of the detector enable the reconstruction of several muon parameters. Muons follow a straight track in the scintillating volume, continuously losing energy through ionization until they stop. The

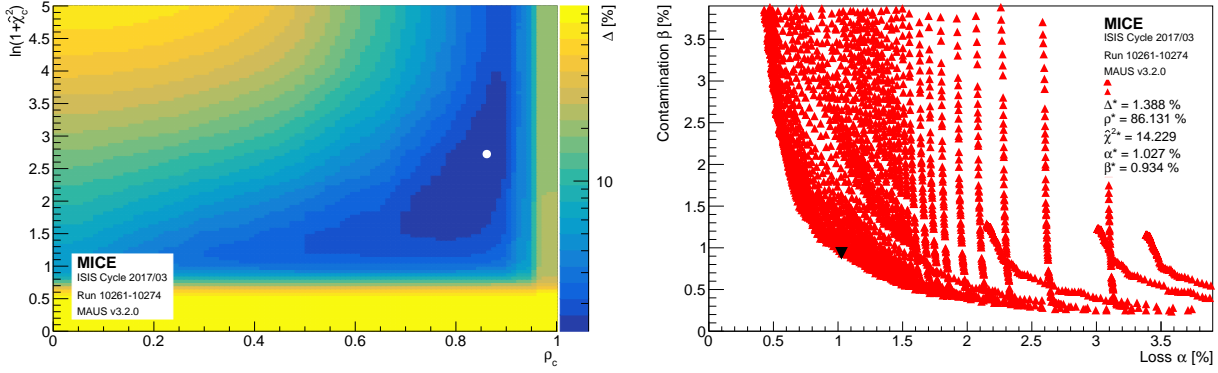


Figure 28: (Left) Cost function,  $\Delta = \sqrt{\alpha^2 + \beta^2}$ , as a function of the choice of cuts on the plane density and shower spread,  $(\rho_c, \hat{\chi}_c^2)$ . The white circle represents the minimum. (Right) Percentage of the electron sample tagged as muons ( $\beta$ ) as a function of the loss of real muons ( $\alpha$ ).

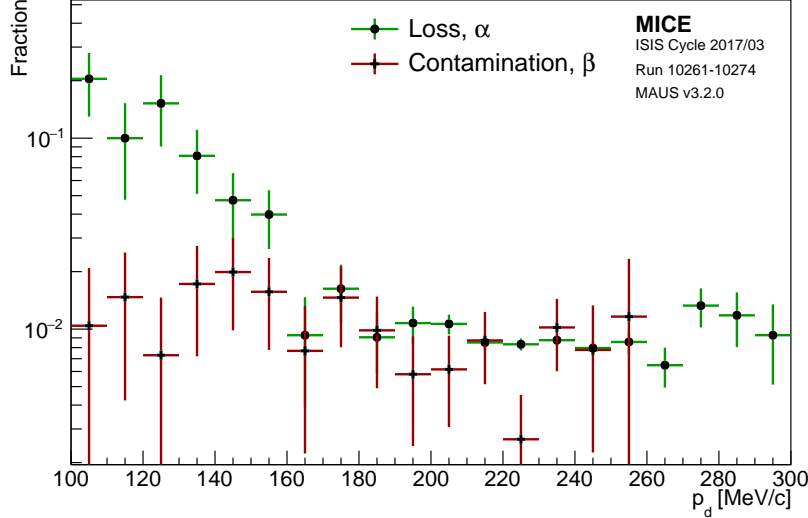


Figure 29: Percentage of electron contamination,  $\beta$ , and muon loss,  $\alpha$ , for different ranges of momentum measured in the downstream tracker,  $p_d$ . The error bars are based on the statistical uncertainty in a bin.

reconstructed track points are fitted with a straight line. The data summarized in table 5 is used to assess the tracking capability of the EMR. The left panel of figure 30 shows the distribution of origin track points, i.e. track positions at the entrance of the detector. The right panel shows the angular distribution of tracks, with respect to the  $z$  axis, as a function of the momentum reconstructed in the downstream tracker.

The end point of a muon track is reconstructed as the final space point in the most downstream plane reached by the particle. The length of the straight track that joins the origin of the track and its end point estimates the muon range. Figure 31 shows the range of muons in the EMR for different data sets and as a function of the momentum reconstructed from the muon time-of-flight between TOF1 and TOF2, i.e.

$$p_{12} = \frac{m_\mu c}{\sqrt{(ct_{12}/d)^2 - 1}}, \quad (9)$$

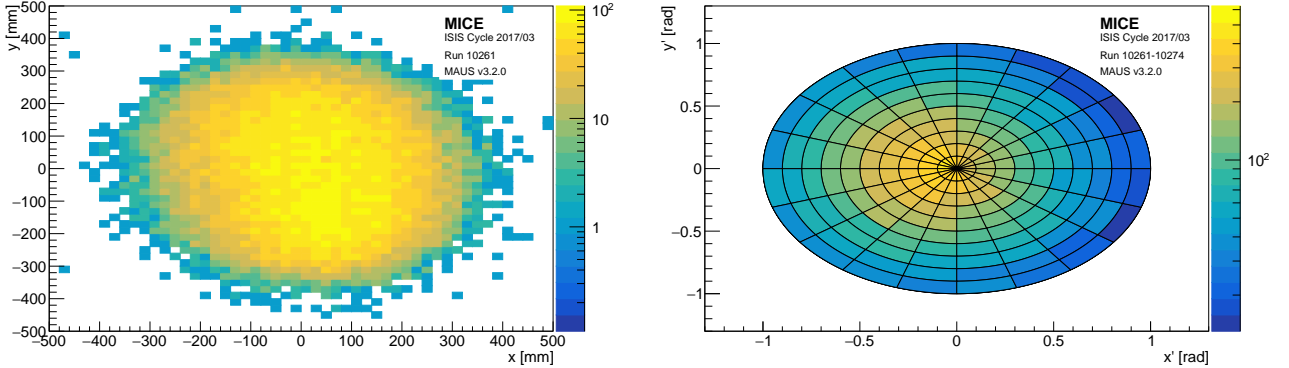


Figure 30: (Left) Beam profile at the entrance of the EMR. (Right) Polar plot of the track gradients in the EMR. The radial excursion represents the angle with respect to the  $z$  axis and the angle represents the azimuth.

with  $m_\mu$  the muon mass,  $t_{12}$  the time-of-flight and  $d$  the distance between the two TOF stations.

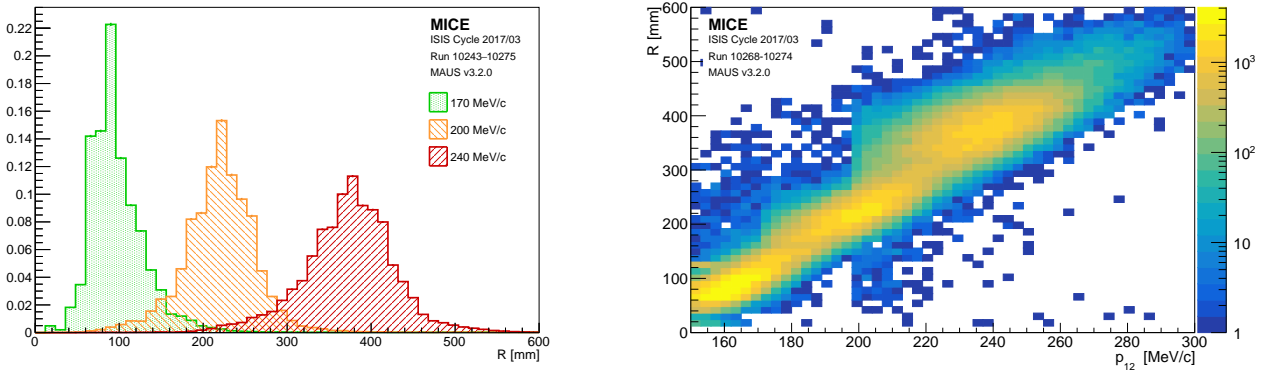


Figure 31: (Left) EMR range distributions of the data sets in the range 170–240 MeV/c. (Right) EMR range as a function of the momentum reconstructed from the time-of-flight between TOF1 and TOF2.

In the muon hypothesis, the Continuously Slowing Down Approximation (CSDA) is used to estimate the muon momentum from its range in polystyrene, the active material of the detector. The range of a muon,  $\mathcal{R}$ , in the CSDA simply reads

$$\mathcal{R} = \int_{T_0}^0 \frac{dE}{|dE/dx|} = \int_{p_0}^0 \frac{dp}{|dE/dx|} \beta c, \quad (10)$$

with  $T_0$ ,  $p_0$  the kinetic energy and momentum of the impinging momentum and  $dE/dx$  the mean ionization energy loss. The impinging momentum,  $p_0$ , may be recovered by numerically inverting equation 10. The momentum reconstructed from the time-of-flight between TOF1 and TOF2,  $p_{12}$ , is propagated to the entrance of the EMR by subtracting the energy lost in TOF2 and the KL. This provides an estimate of  $p_0$  that may be used to validate the momentum reconstruction in the EMR, as shown in figure 32.

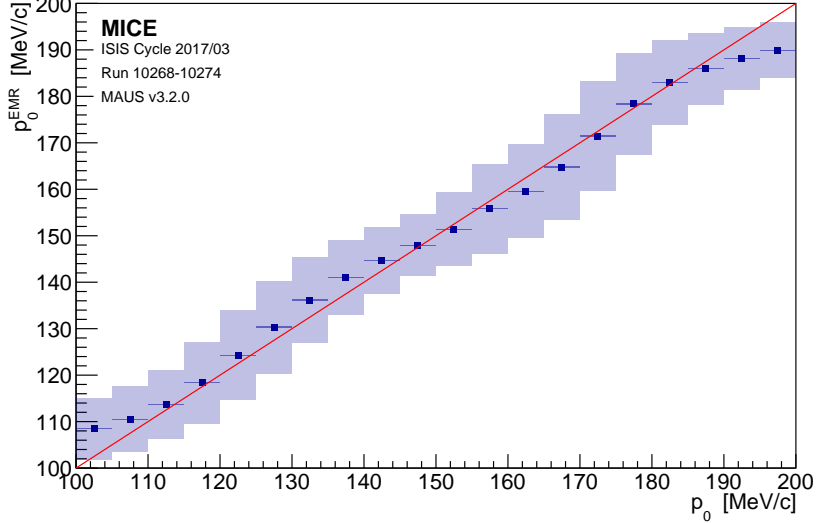


Figure 32: Momentum reconstructed in the EMR as a function of the momentum estimated at the entrance of the EMR from the time-of-flight information. The markers represent the mean in the bin, the dark band the uncertainty on the mean and the light band the RMS. The red line represents perfect agreement.

## 400 6 Trackers

### 6.1 Introduction

MICE is equipped with two identical, high precision scintillating-fibre trackers, described in [16]. Each tracker is placed in a superconducting solenoid designed to provide a uniform magnetic field over the tracking volume. One tracker, TKU, is upstream of the cooling cell, the other, TKD, is downstream, the mirror image of TKU as 405 in Fig. 1.

The trackers are 110 cm in length and 30 cm in diameter (see Fig. 33). There are five stations per tracker (labelled 1 to 5, with station 1 being closest to the cooling cell) held in position using a carbon-fibre space-frame. The stations sit at varying separations in  $z$  (beam axis) of 20–35 cm: this ensures that the azimuthal rotation 410 of track position from one station to the next differs, difference being important in resolving ambiguities at the pattern-recognition stage. Each tracker is instrumented with an internal LED calibration system for calibration and four 3-axis Hall probes to monitor the field.

The tracker stations consists of three doublet layers of  $350\mu m$  scintillating fibres, these layers are arranged such that each is at an angle of  $120^\circ$  to the next. This arrangement ensures that there are no inactive regions between adjacent fibres. Bundles of seven fibres are grouped into a single readout channel (this reduces the 415 number of readout channels, while maintaining position resolution). The trackers have a spatial resolution per doublet layer of  $470\mu m$  and an expected light yield of  $\sim 10$  photo-electrons.

The light from the seven scintillating fibres passes into a single clear fibre, which takes it to a visible light photon counter (VLPC) which operate at 9 k. The signals from the VLPCs are digitised using electronics developed by the D0 collaboration [17].



Figure 33: Photograph of one of the MICE Trackers, showing the five stations and the three doublet planes of scintillating fibres, each plane at 120° angles to the next (the central fibres of plane can be seen as darker lines traversing the station). Bundles of seven  $350\mu m$  fibres are grouped together, to be read out by 1 mm scintillating fibre light guides.

## 420 6.2 Tracker Performance and Reconstruction

### 6.2.1 Low Level Analysis

In order to validate the performance of the tracker and its reconstruction it is necessary to validate each element of the reconstruction which goes into creating the final particle tracks through the tracker. This is known as low level analysis.

425 Each of the 15 tracker planes (three per station and five stations) consist of 214 channels, labelled 0–213, likewise each plane is assigned an integer plane number 0–2. Particle signals are recorded by the tracker electronics and calibrated channel by channel then converted into signal NPE. This information is then used to form a digit and is the first step in tracker reconstruction.

430 In Fig. 34 and Fig. 35 are shown the digit profiles for each of the 15 planes (with planes 0–2 shown in columns left to right and each plane of stations 1–5 shown in descending rows) respectively for TKU and TKD. These digit profiles are useful in identifying and rectifying or removing hot or dead channels in the planes and ensuring the accuracy of calibration. Smooth centrally peaked spectra are expected in a plane with no dead channels and minimal electronics noise, but this is not an essential requirement since it is the combination of two or three planes which go to make a point in the track and so there is redundancy built in. Hence a significant proportion of individual channels can be lost without a knock on drop in efficiency.

435 A number of channels in the readout electronics were lost due to ageing over the summer shut down. The effect was minimised by re-routing the external light-guides to allow the channels which could not be read out to be grouped into one plane per station.

The clustering algorithm loops over every combination of pairs of digits in a single event and combines any 440 that occur in neighbouring channels. In the case of a multi-digit cluster, the unweighted average channel value is used to define the plane coordinate and the NPE is summed.

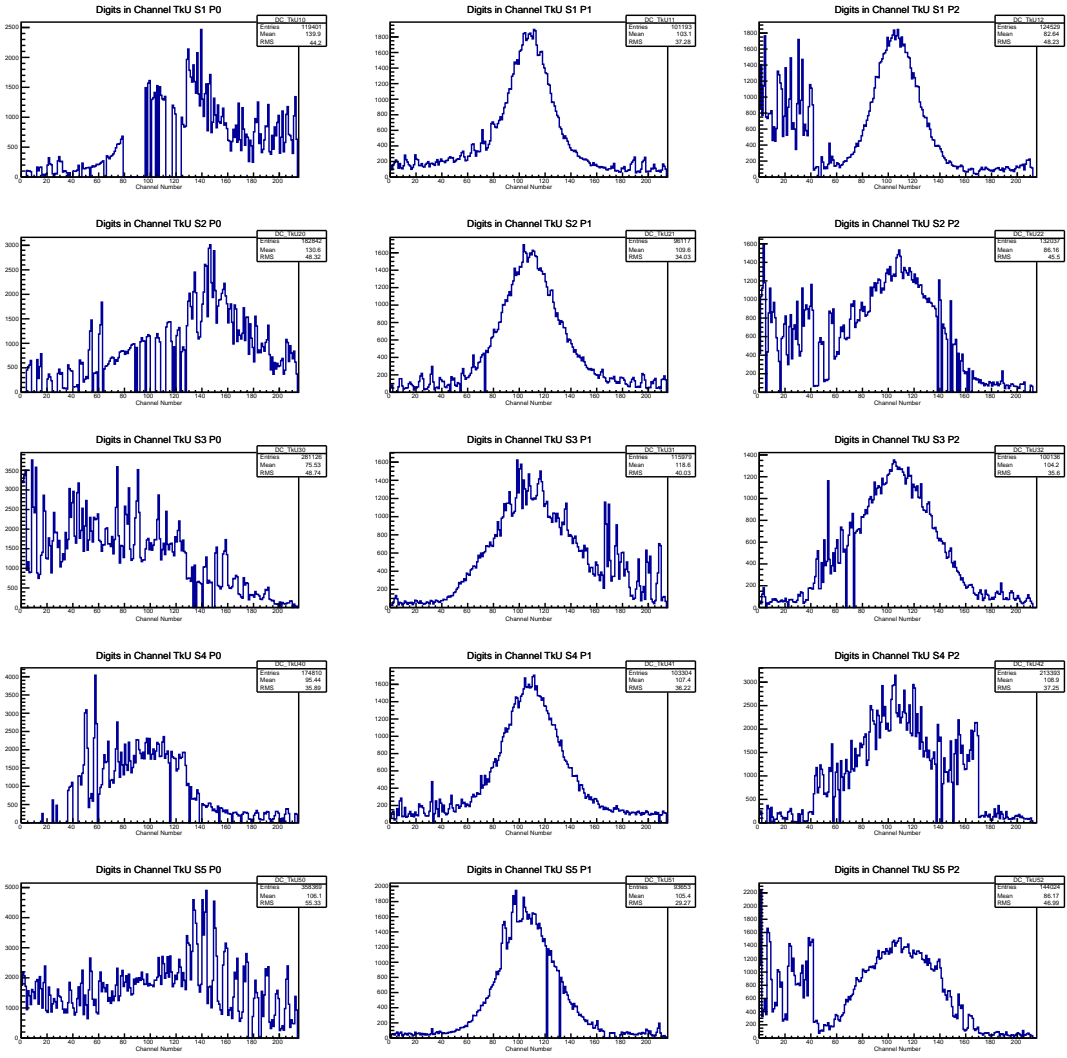


Figure 34: Digit profiles for the 15 planes of TKU, showing total NPE deposited for all events against channel number in the tracker plane.

For each station the constituent planes are searched for clusters that can be used to form a spacepoint. Spacepoints are constructed from clusters from all three planes (a triplet spacepoint) or from any two out of the three planes (a doublet spacepoint), as shown in Fig. 38 and Fig. 39 respectively for TKU and TKD.

### 445 6.2.2 Noise

The scintillating fibre trackers operate by registering digits above a given NPE threshold within each fibre plane. Fibres are collected into channels as ganged bundles of 7 for each channel, with digits registered per channel instead of per fibre. From a coincidence of digit events in 2 or 3 oblique fibres (fibres in differing planes), a spacepoint is reconstructed, from which track reconstruction can occur. We consider noise in the tracker to be those digits registered not from the passage of a beam particle, but instead from other sources, for instance, dark current from thermal electron emission in the PMTs. To isolate noise from signal during beam-on data collection, a strict cut can be made requiring that only events with one fitted track and 5 spacepoints per tracker are selected, with all 5 spacepoints included in the fitted track. All digits corresponding to the track are then

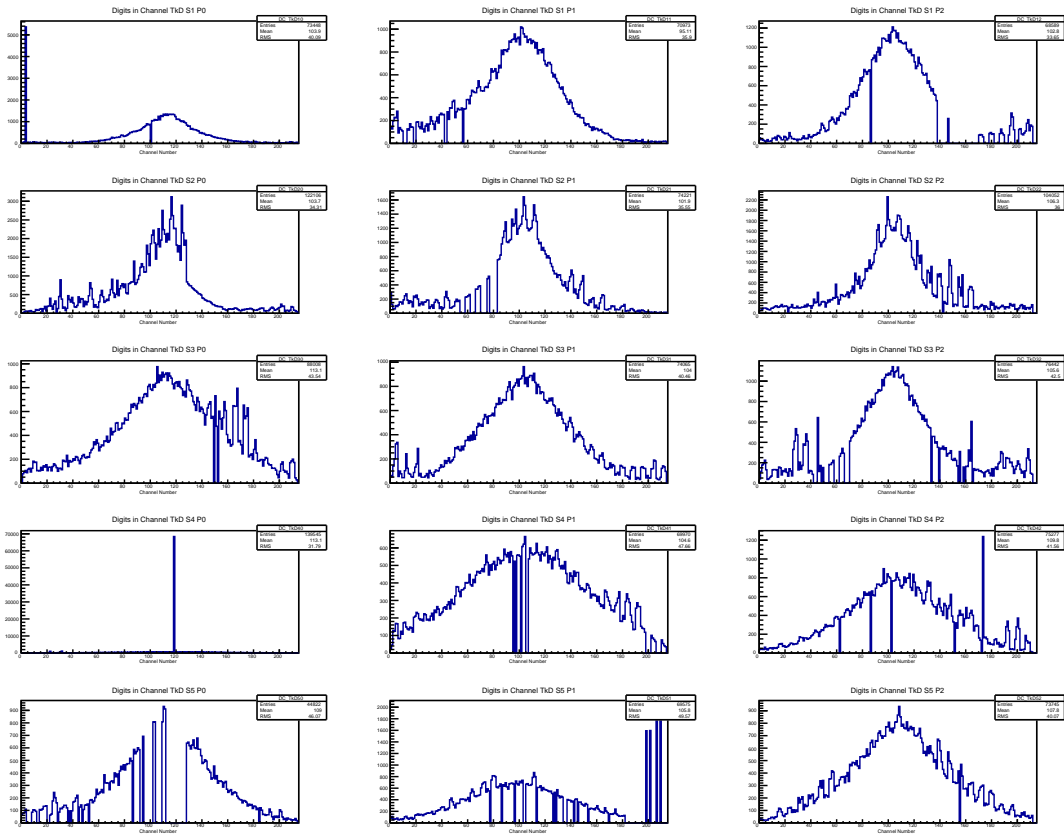


Figure 35: Digit profiles for the 15 planes of TKD, showing total NPE deposited for all events against channel number in the tracker plane.

removed from the total set of digits for that event, and the remainder are considered noise digits. An in-situ approximation of active channels for the current data-taking period is made, assuming all channels without at least one registered digit in the selected data-taking run are inactive. The average noise rate per channel per event is then calculated as the total number of event digits above the considered NPE threshold in each tracker, divided by both the active channel number and the number of events satisfying the above selection criteria. This gives a value of 0.18% upstream and 0.06% downstream for events above 2 NPE.

### 460 6.2.3 Track Finding Efficiency

Data were analysed in order to determine the track and spacepoint finding efficiency of the detectors during running conditions. A time-of-flight cut was used to ensure that each measured track had a time-of-flight consistent with a muon throughout the entire experimental apparatus (see Fig. 40). A hit was therefore required in each of the TOF1 and TOF2 detectors, which ensured that the particle must have been successfully transmitted through the cooling channel, crossing both tracking detectors. These requirements ensure that there is a better than 99.9% probability that a particle will have traversed a tracking detector. The number of events missing a track is therefore measured and used to estimate the efficiency of the detector.

The results of the efficiency analysis are tabulated in table 6 for a range of momentum and nominal emittances. A track-finding efficiency of 98.70% is reported for the upstream tracker and 98.93% for the downstream tracker, averaged over field and beam conditions. Additionally, assuming a track is found, the probability of successfully finding each spacepoint is summarized in table 7. The overall efficiency of both trackers

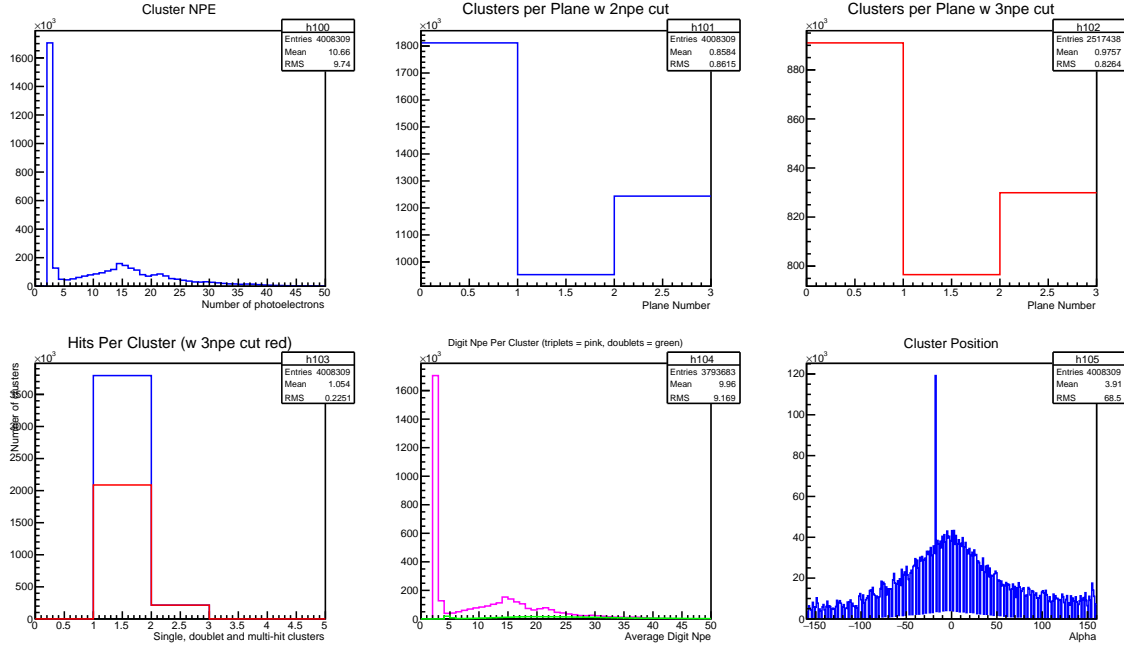


Figure 36: Cluster

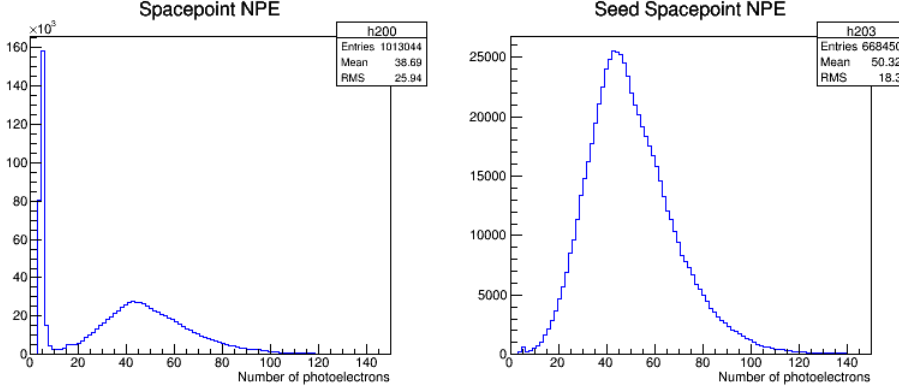


Figure 37: (Left) the NPE of each spacepoint in the US and DS trackers combined. (Right) only the NPE of those spacepoints which go on to make tracks in the US and DS trackers combined are shown.

is sufficient to not present any significant systematic uncertainties in the analysis, however it is lower than the ideal expectation, 99.9% efficiency, due to the presence of dead channels, an unavoidable feature of the construction process.

#### 475 6.2.4 Track Fit Predicted Performance

Monte Carlo simulation used with realistic field and beam conditions in order to estimate the reconstruction performance. Run number 09964 was used (140 MeV/c, 10 mm nominal emittance), representing a typical data set used for the study of emittance evolution. Results are presented in Fig. 41 for the upstream tracker and Fig. 42 for the downstream tracker.

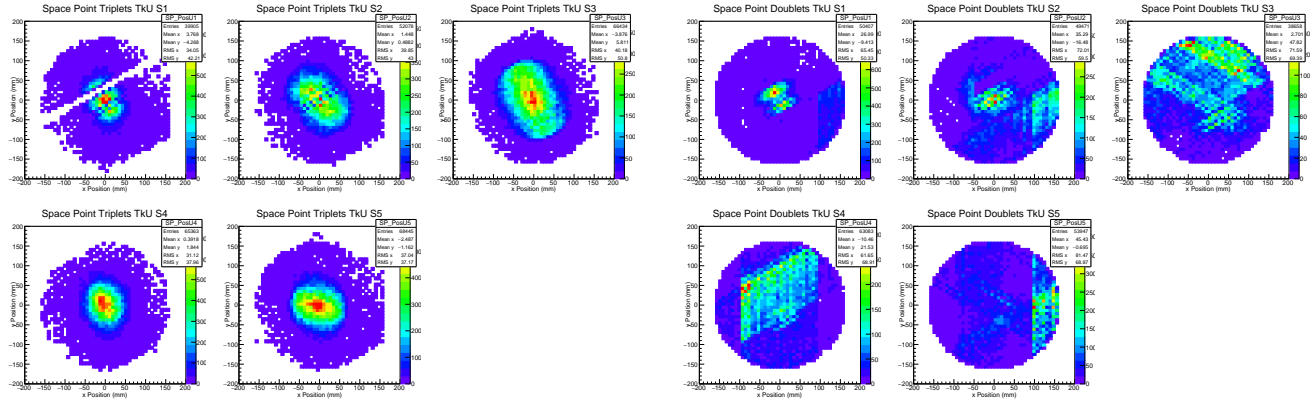


Figure 38: Space point triplets in TKU (left) and in TKD (right).

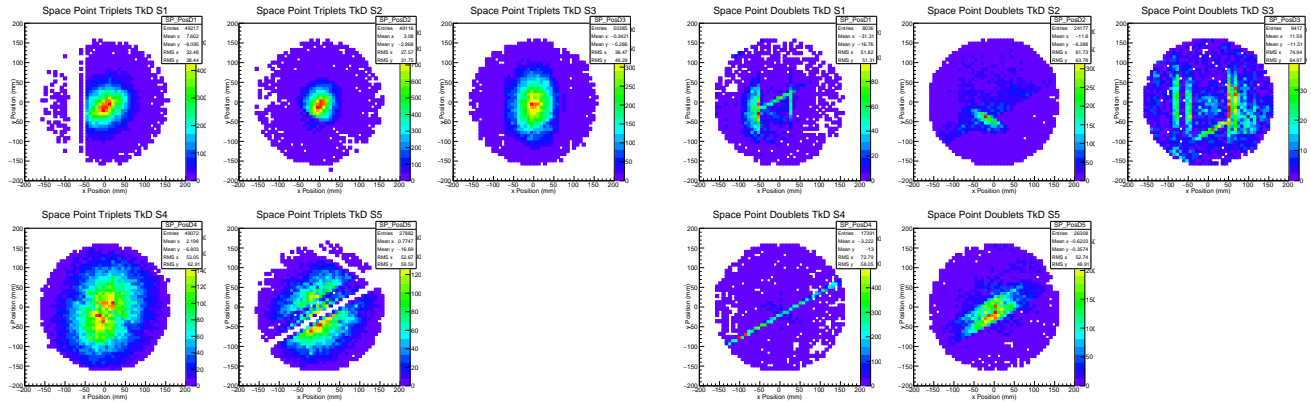


Figure 39: Space point doublets in TKU (left) and in TKD (right).

### 480 6.3 Tracker Efficiency Evolution

The efficiency of the tracker was processed over the lifetime of its use during the data taking. The analysis used in section 6.2.3 was repeated and automated for runs starting in 2015. The evolution of the helical track finding efficiency in the upstream and downstream trackers is shown in Fig. 43.

## 7 Particle ID

- 485 While the protons in the MICE beam can be effectively removed before entering the detectors [18], the remaining particles are a mix of pions, muons, and electrons. Effective particle ID (PID) methods are required to ensure that we are measuring the cooling of muons rather than of other particle species. While earlier studies in MICE were performed with a beam optimized for muon purity [8], accurate particle ID algorithms allow us to optimize for muon yield rather than purity.

490 **Work is ongoing on an alternate multivariate likelihood-based PID algorithm, but the currently-used cut-based algorithm will be described here.**

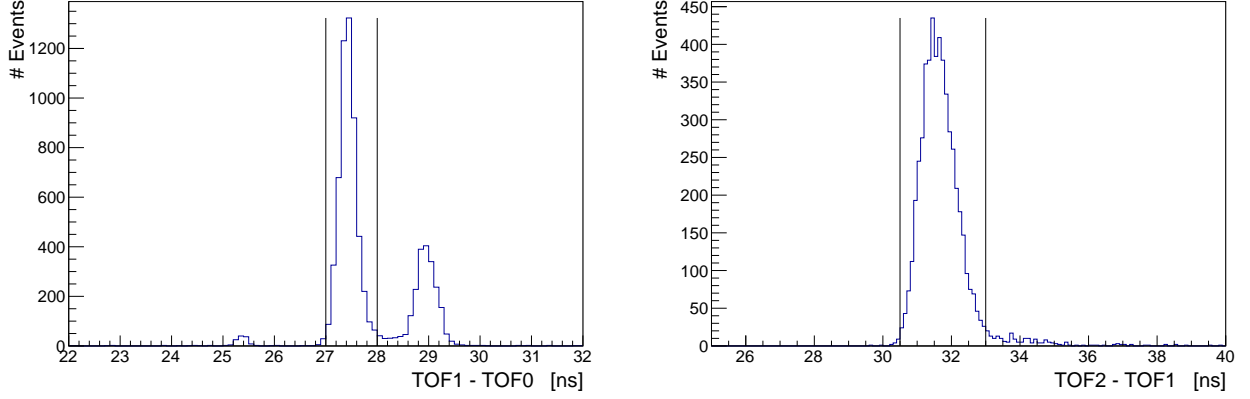


Figure 40: Time-of-flight distributions between TOF0 and TOF1 (left) and between TOF1 and TOF2 (right) for run number 09768. The location of the cuts is shown. The left plot demonstrates the event selection before entering the cooling channel and the right plot demonstrates the impurity rejection.

Momentum	Nominal Emittance	No. Events	Upstream Tracks Found	Downstream Tracks Found
200 MeV/c	6mm	221879	99.42%	96.07%
200 MeV/c	3mm	215229	98.38%	99.19%
140 MeV/c	6mm	180283	98.37%	99.16%
140 MeV/c	10mm	130859	98.47%	98.93%
Averaged		748250	98.70%	98.21%

Table 6: The track finding efficiency for the upstream and downstream trackers for 140 MeV/c and 200 MeV/c beams, and for 3, 6 and 10 mm nominal emittances.

## 7.1 Algorithm

The PID algorithm uses the TOF and Tracker detectors. TOF0 and TOF1 can be combined with the upstream tracker to ID a particle upstream of the absorber. However, if the particle has decayed while travelling through the detector, a downstream identification is more difficult due to the fact that there is no entirely-downstream TOF measurement. TOF1 and TOF2 can be combined with the downstream tracker, but the uncertainty in the PID is increased due to the particles' energy loss in the absorber.

A particle's momentum can be calculated by the curvature of its track in the tracker's solenoid field, while its velocity can be calculated from the time-of-flight and the path length. From these, the particle's mass can be calculated:

$$m = \frac{p\sqrt{1 - (v/c)^2}}{v/c} \quad (11)$$

the particle can then be determined to be a pion ( $m = 140$  MeV), muon ( $m = 105$  MeV) or electron ( $m = 511$  keV).

This method requires an accurate measurement of the particle's path length between the TOF detectors, which will be slightly longer than the straight-line distance between the detectors due to the magnetic fields involved. The time-of-flight of electrons is used to calibrate this distance, since electrons are moving very close to the speed of light ( $\gamma \approx 500$ ) at these beam momenta. Therefore, after a fit of the electron TOF peak in a particular beam setting, each particle's  $v/c$  is calculated as  $TOF_e/TOF$ .

Additionally, this calculation assumes that the measurements of TOF and momentum were performed at the

Momentum	Nominal Emittance	No. Events	Upstream Spacepoints Found	Downstream Spacepoints Found
200 MeV/c	6mm	221879	99.41%	94.63%
200 MeV/c	3mm	215229	98.04%	97.41%
140 MeV/c	6mm	180283	97.99%	99.16%
140 MeV/c	10mm	130859	98.07%	97.44%
Averaged		748250	98.44%	97.01%

Table 7: The spacepoint finding efficiency, assuming the presence of a track, for the upstream and downstream trackers for 140 MeV/c and 200 MeV/c beams, and for 3, 6 and 10 mm nominal emittances.

same point. Since the particle has lost momentum between the TOF and Tracker detectors, a correction must be added. Figure 44(a) shows that before this correction, the data points are well-separated into different particle species, but are slightly displaced from their naively-expected positions.

To find this correction, a loose cut is performed on the data to find particles that are near the muon mass. A fit is performed on these particles to find a momentum offset to be applied in Equation 11 to ensure that the muons are centred at the muon mass of 105.7 MeV. Figure 44(b) shows the same data as in (a), but the expected pion and muon curves have been adjusted with this momentum offset.

After the above parameters  $\text{TOF}_e$  and  $p_{\text{offset}}$  have been found, the PID algorithm can be applied to each track to calculate a mass for the particle, as shown in Figure 45. Analyses may require different cuts on this variable due to different purity requirements, but pions and muons are sufficiently well-separated to allow good identification.

## 7.2 Performance of the PID

- add efficiency/purity curve
- compare US/DS measurements

## 8 Global Track Matching reconstruction

The overall detector performance can be validated by extrapolating tracks from one detector to another and comparing the reconstructed coordinates with the extrapolated values. Tracks measured in the upstream tracker are extrapolated upstream to TOF1 and TOF0, and downstream to TKD and TOF2. Where there are materials in the beamline, the energy change on passing through the material is estimated using the most probable energy loss. Material thicknesses are approximated by the on-axis thickness.

Asymmetric effects can be introduced due to scattering from the walls of the cooling channel as the beam is not symmetric in the channel. In order to minimise the effects of such scattering, only events whose projected trajectory is significantly distant from the apertures are considered in this analysis. The following sample selection is considered:

- Downstream sample: events must be included in the downstream sample to be considered in this analysis
- Aperture cut: the projected upstream track must be within 100 mm radius from the beam axis at the following apertures: the upstream absorber safety window; the upstream absorber window; the absorber centre; the downstream absorber window; the downstream absorber safety window; the upstream edge of SSD; the Helium window in SSD; the downstream edge of the downstream PRY aperture. This is performed even when the LH2 absorber was not installed, for the sake of consistency and because in some instances mounting flanges can limit the aperture and consistency.

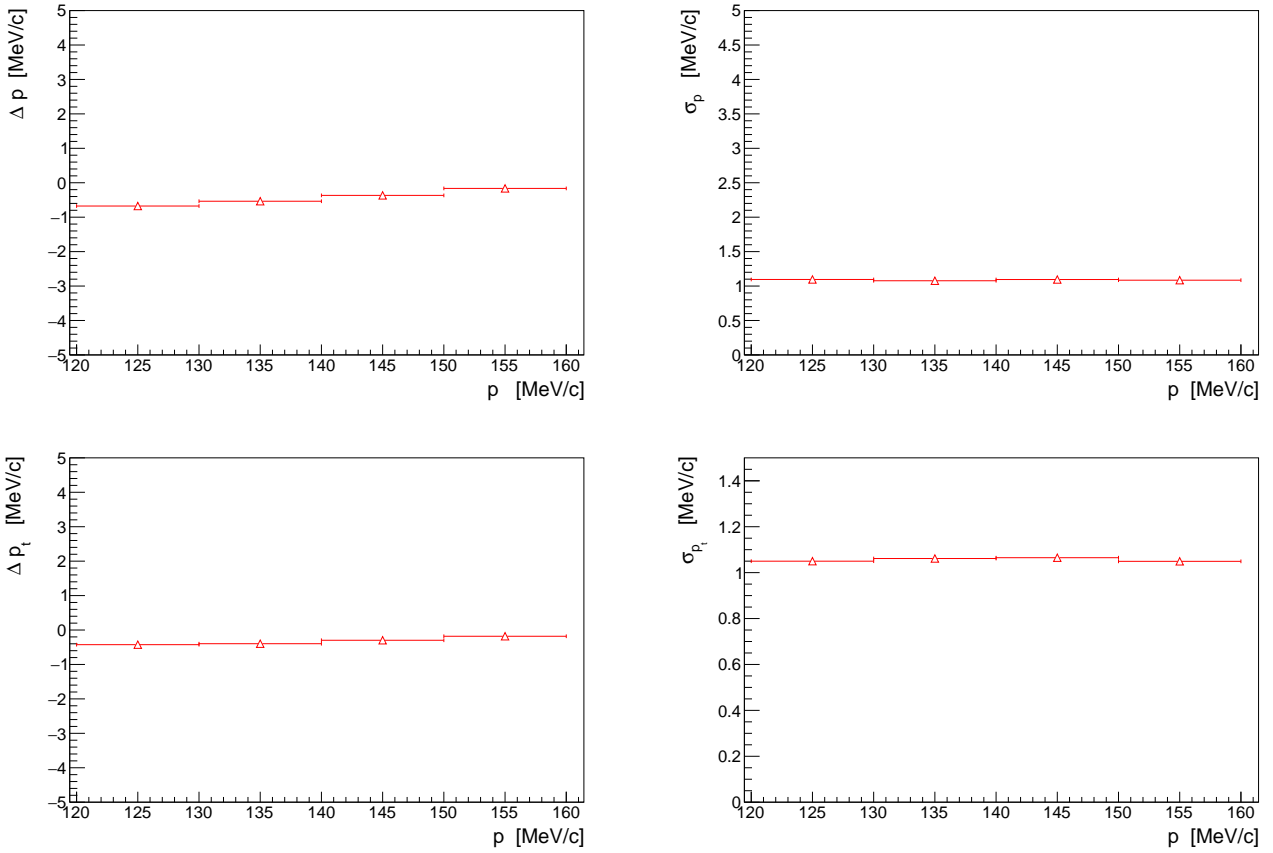


Figure 41: Predicted momentum reconstruction bias (left) and resolution (right) for the longitudinal (top) and transverse (bottom) momentum components in the upstream tracker.

540

- 1 space point in TOF2: the event must have exactly one space point in TOF2.
- Successful track extrapolation to TOF2: the projected upstream track must have been successfully extrapolated to TOF2

The sample sizes are shown for data in table 8 and 9. The equivalent MC sample sizes are listed in 10 and 11.

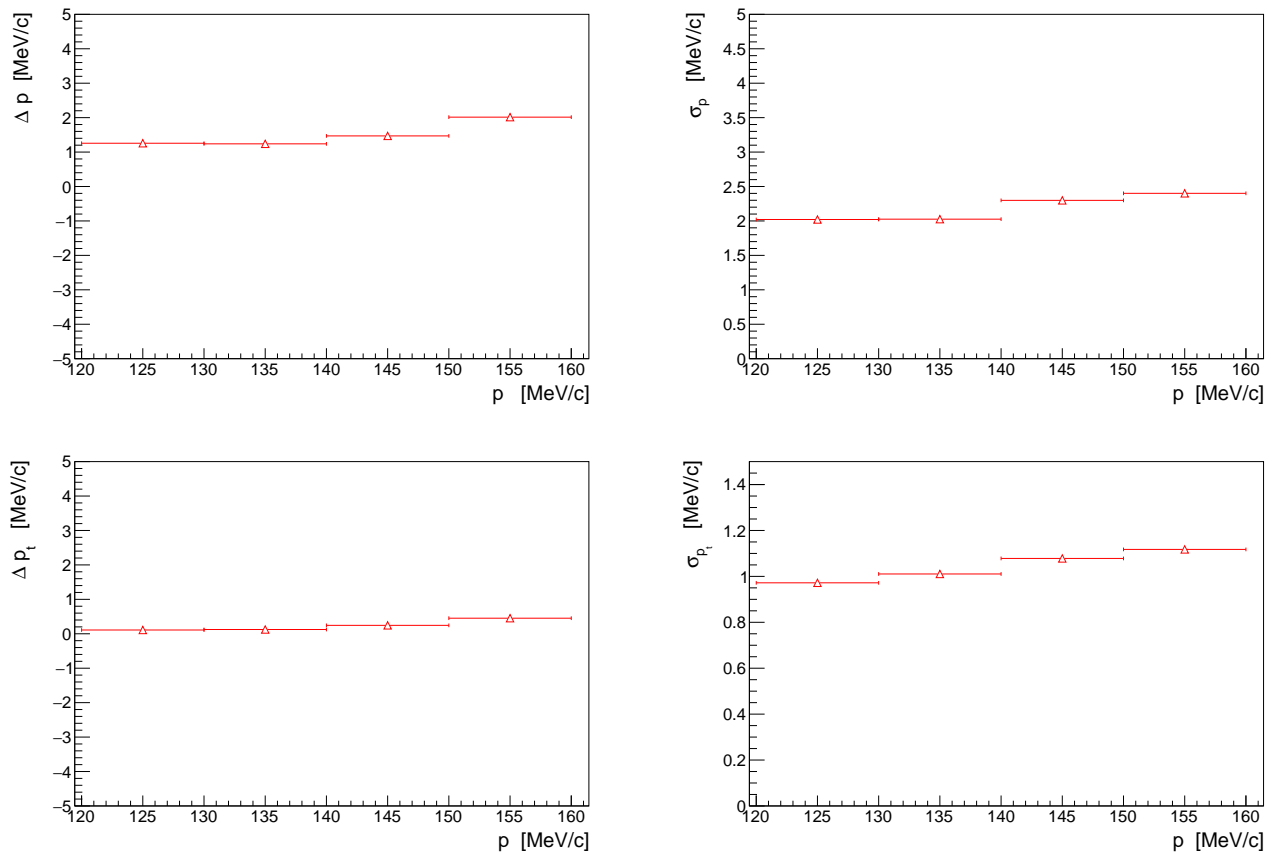


Figure 42: Predicted momentum reconstruction bias (left) and resolution (right) for the longitudinal (top) and transverse (bottom) momentum components in the downstream tracker.

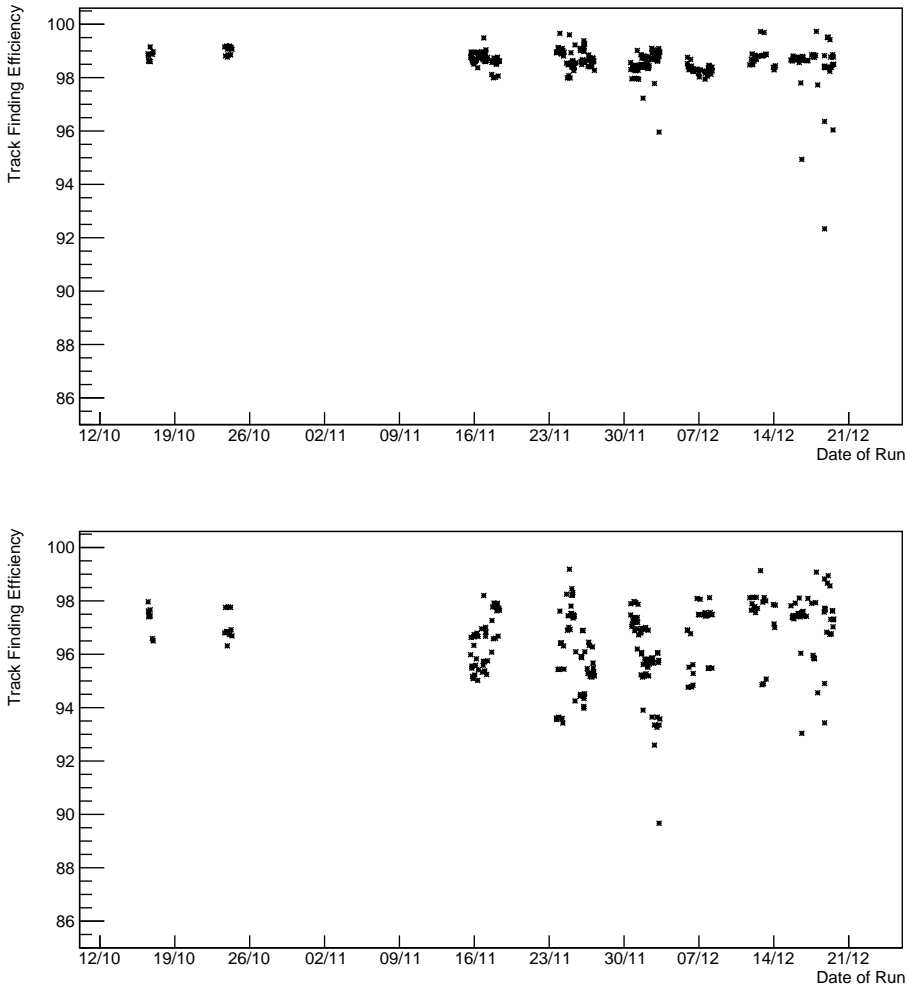


Figure 43: Evolution of the helical track finding efficiency over time for the upstream (top) and downstream (bottom) trackers during the key periods of data taking in 2016.

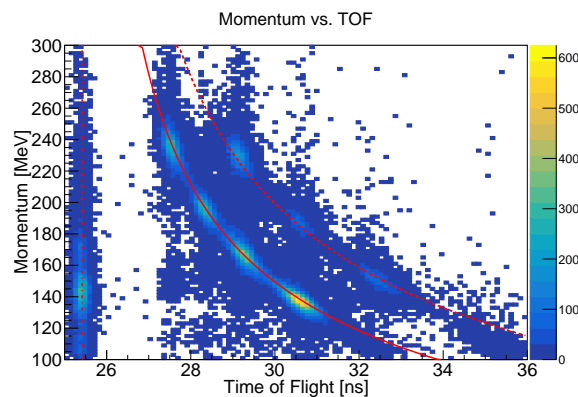


Figure 44: The TOF measurement and Tracker momentum of particles in a selection of MICE runs with different momentum settings for the beam. The lines shows the expected momentum vs. TOF for pions at  $m = 140$  MeV, muons at  $m = 105$  MeV and electrons at  $m = 511$  keV. The expected relation is shown after correcting for this energy loss.

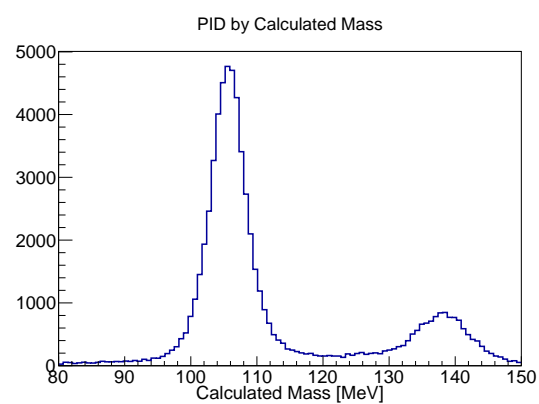


Figure 45: The calculated mass of particles using the PID algorithm.

Table 8: The extrapolated reconstructed data sample is listed. Samples are listed for 3-140 and 4-140 datasets.

	2017-2.7 3-140 None	2017-2.7 3-140 IH2 empty	2017-2.7 3-140 IH2 full	2017-2.7 3-140 LiH	2017-2.7 4-140 None	2017-2.7 4-140 IH2 empty	2017-2.7 4-140 IH2 full	2017-2.7 4-140 LiH
Downstream Sample	13019	8688	9058	11918	29712	23726	8407	24024
Cooling channel aperture cut	7203	4721	5166	6836	17731	14571	4935	14293
One space point in ToF2	6935	4506	4885	6477	16800	13817	4596	13362
Successful extrapolation to TKD	6935	4506	4885	6477	16800	13817	4596	13362
Successful extrapolation to ToF2	6935	4506	4885	6477	16800	13817	4596	13362
Extrapolation Sample	6935	4506	4885	6477	16800	13817	4596	13362

Table 9: The extrapolated reconstructed data sample is listed. Samples are listed for 6-140 and 10-140 datasets.

	2017-2.7 6-140 None	2017-2.7 6-140 IH2 empty	2017-2.7 6-140 IH2 full	2017-2.7 6-140 LiH	2017-2.7 10-140 None	2017-2.7 10-140 IH2 empty	2017-2.7 10-140 IH2 full	2017-2.7 10-140 LiH
Downstream Sample	27025	17783	29577	31257	14847	7278	14784	17138
Cooling channel aperture cut	15238	10129	16045	17122	5633	2837	5057	6075
One space point in ToF2	14432	9479	14826	15774	5276	2614	4471	5372
Successful extrapolation to TKD	14432	9479	14826	15774	5276	2614	4471	5372
Successful extrapolation to ToF2	14432	9479	14826	15774	5276	2614	4471	5372
Extrapolation Sample	14432	9479	14826	15774	5276	2614	4471	5372

Table 10: The extrapolated reconstructed simulated sample is listed. Samples are listed for 3-140 and 4-140 datasets.

	Simulated 2017-2.7 3-140 None	Simulated 2017-2.7 3-140 IH2 empty	Simulated 2017-2.7 3-140 IH2 full	Simulated 2017-2.7 3-140 LiH	Simulated 2017-2.7 4-140 None	Simulated 2017-2.7 4-140 IH2 empty	Simulated 2017-2.7 4-140 IH2 full	Simulated 2017-2.7 4-140 LiH
Downstream Sample	8585	8567	8511	8624	18247	18247	18455	18553
Cooling channel aperture cut	5112	4715	5032	5378	10884	10997	10758	10404
One space point in ToF2	4540	4184	4499	4820	9544	9747	9467	9117
Successful extrapolation to TKD	4540	4184	4499	4820	9544	9747	9467	9117
Successful extrapolation to ToF2	4540	4184	4499	4820	9544	9747	9467	9117
Extrapolation Sample	4540	4184	4499	4820	9544	9747	9467	9117

Table 11: The extrapolated reconstructed simulated sample is listed. Samples are listed for 6-140 and 10-140 datasets.

	Simulated 2017-2.7 6-140 None	Simulated 2017-2.7 6-140 IH2 empty	Simulated 2017-2.7 6-140 IH2 full	Simulated 2017-2.7 6-140 LiH	Simulated 2017-2.7 10-140 None	Simulated 2017-2.7 10-140 IH2 empty	Simulated 2017-2.7 10-140 IH2 full	Simulated 2017-2.7 10-140 LiH
Downstream Sample	17810	18031	18188	18259	8843	9029	9155	9294
Cooling channel aperture cut	10289	10071	9449	9906	3424	3393	3227	3337
One space point in ToF2	9014	8766	8219	8577	2941	2926	2772	2861
Successful extrapolation to TKD	9014	8766	8219	8577	2941	2926	2772	2861
Successful extrapolation to ToF2	9014	8766	8219	8577	2941	2926	2772	2861
Extrapolation Sample	9014	8766	8219	8577	2941	2926	2772	2861

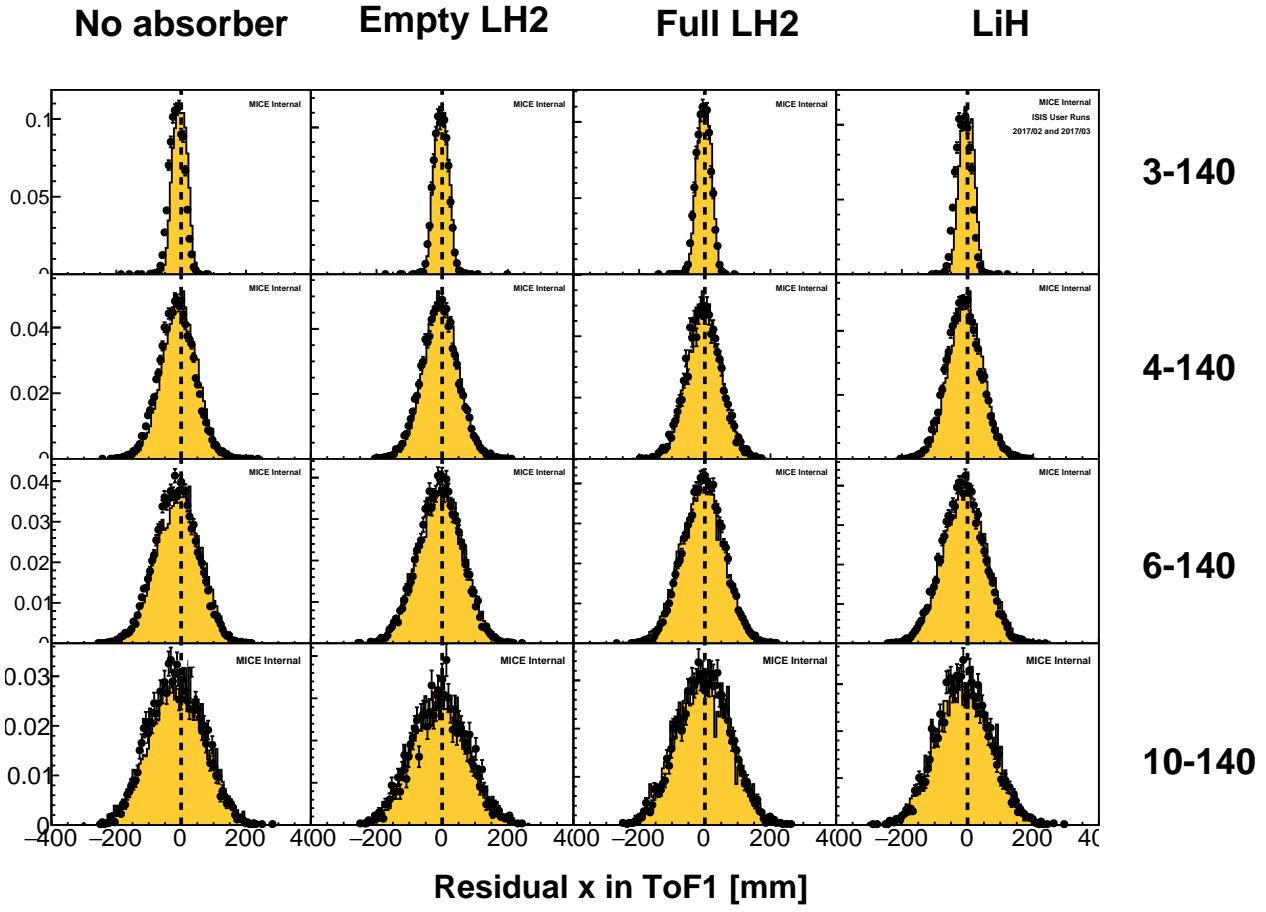


Figure 46: Residual horizontal (x) position in TOF1 of tracker tracks following extrapolation from TKU.

545 A typical residual plot is shown in Fig. 46 for the extrapolated position following extrapolation to TOF1. In general the width of the distributions are comparable between MC and data. Where the diffuser is in place for higher emittance beams, the extrapolation goes through the diffuser material so the residuals are wider, owing to the increased scattering from the diffuser.

## 9 Beam-based detector alignment

550 To carry out its program, MICE requires all of its detectors to reconstruct space points in a globally consistent fashion. A beam-based alignment algorithm was developed to improve the resolution on the position of the scintillating-fibre trackers lodged inside the bores of superconducting magnets. This method can achieve unbiased measurements of the trackers rotation angles with a resolution of  $6 \text{ mrad}/\sqrt{N}$  and of their position with a resolution of  $20 \text{ mm}/\sqrt{N}$ , with  $N$  the number of selected tracks. This section briefly describes the alignment 555 algorithm and presents the results obtained during the 2017/01 ISIS user cycle as an example case. The procedure is described in greater details and cross-checked on several simulations in [19].

## 9.1 Introduction

The single-particle nature of the MICE experiment requires reliable global track matching throughout, i.e. the ability to associate a trace measured in the upstream tracker with one in the downstream tracker but also with the particle identification detectors. The many detectors must reconstruct space points in a globally consistent fashion to guarantee reliable and efficient track matching, as well as unbiased muon scattering measurements.

The baseline for the beam-based alignment is the surveys of the detectors in the hall using laser telemetry. Surveys were performed regularly throughout the MICE Step IV commissioning phase and data taking period. The TOF1 time-of-flight hodoscope was moved periodically to access the upstream end of the superconducting solenoids and resurveyed systematically. The downstream particle identification detectors module, composed of TOF2, the KL and the EMR, was also repositioned on occasion. The focus coil module was moved in and out of the beam line to change absorbers. Each of these events was followed by a complete resurvey.

The particle identification detectors are each equipped with at least four survey monuments and are surveyed directly. The two scintillating fibre trackers, nested in the superconducting solenoids, can not be accessed. The upstream and downstream flanges of each solenoid are surveyed and the end plate of the trackers are surveyed with respect to the flanges. The estimated position of the trackers within the bores are inferred from these measurements. A laser theodolite is used to locate the monuments with respect to the datum point situated under the second dipole magnet, D2. Figure 47 shows a picture of TOF2 and the location of its survey monuments.

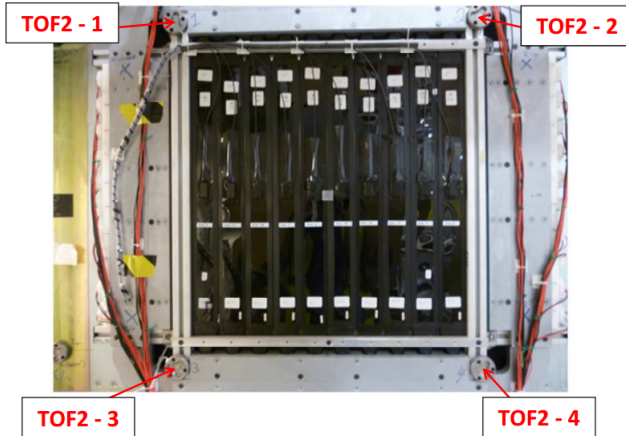


Figure 47: Picture of the TOF2 time-of-flight hodoscope and its four survey monuments labelled TOF2.1–2.4.

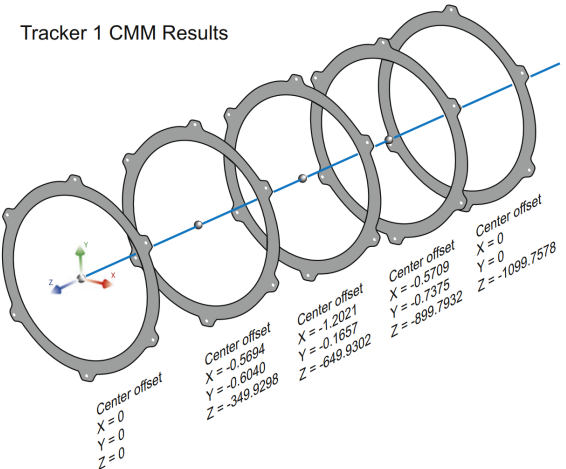


Figure 48: Disposition of the downstream tracker stations along with the CMM measurements of their position with respect to the reference axis.

Before being placed inside the magnets, each tracker was surveyed independently using a coordinate-measuring machine (CMM). This ensures that the position of the five stations is well known within each tracker with respect to the end plate. Figure 48 shows the disposition of the stations in the downstream scintillating fibre tracker and their position as measured by the CMM. The reference position is the axis that joins the centre of station 1 to the centre of station 5. The positions of stations 1 to 3 are measured with respect to that axis. The beam can be used to check the tracker station alignment.

Special care is taken during the installation of the trackers within the magnet bores. The installation platform is adjustable to enable the tracker to be aligned with the bore of the solenoid. The tracker sits on four adjustable feet, two at each end. The adjustable feet are used to align the tracker with the magnetic axis of the solenoid. Once this has been done, the location bracket is fitted. The location bracket locks the tracker in its longitudinal and azimuthal positions.

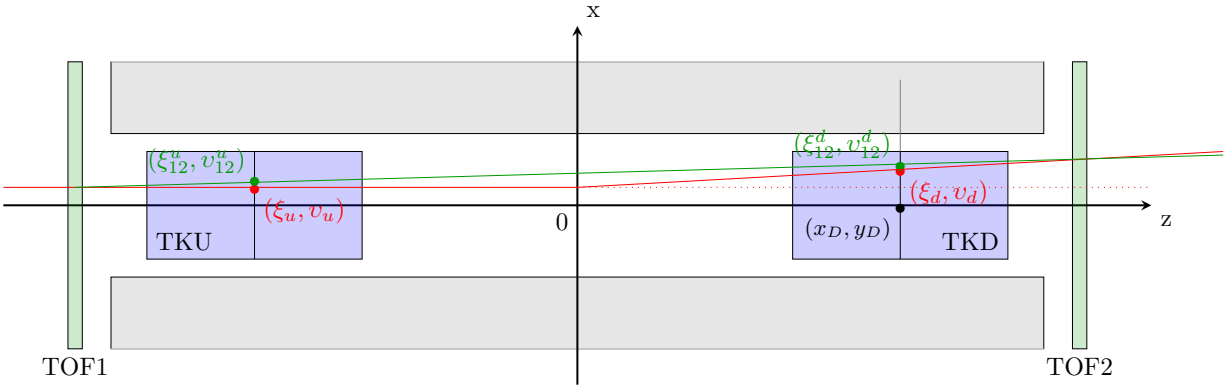


Figure 49: True path of a single particle track (red) and its path as reconstructed from the time-of-flight system (green). The position of the track at the tracker centres is represented by markers.

## 585 9.2 Analysis method

The position of tracker  $t = u, d$  in global coordinates is entirely defined by the location of its centre  $(x_T, y_T, z_T)$  and a set of Tait-Bryan angles  $(\alpha_T, \beta_T, \gamma_T)$ . The  $z$  axis is oriented along the beam line and points downstream, the  $y$  axis points upwards and the  $x$  axis completes the right-handed coordinate system. The rotation about  $x$ ,  $\alpha_T$ , is called pitch, about  $y$ ,  $\beta_T$ , is called yaw and about  $z$ ,  $\gamma_T$ , is called roll. For a straight track of local coordinates  $(x_t, y_t, z_t)$  at the tracker centre, the global coordinates are reconstructed as

$$\begin{pmatrix} \xi_t \\ v_t \\ \zeta_t \end{pmatrix} = \begin{pmatrix} x_t - \gamma_T y_t + \beta_T z_t + x_T \\ y_t + \gamma_T x_t - \alpha_T z_t + y_T \\ z_t - \beta_T x_t + \alpha_T y_t + z_T \end{pmatrix}. \quad (12)$$

in the first order small angles approximation. The global gradients of the straight track thus read

$$\begin{aligned} \xi'_t &= \frac{d\xi_t}{d\zeta_t} = \frac{dx_t - \gamma_T dy_t + \beta_T dz_t}{dz_t (1 - \beta_T x'_t + \alpha_T y'_t)} \simeq x'_t - \gamma_T y'_t + \beta_T, \\ v'_t &= \frac{dv_t}{d\zeta_t} = \frac{dy_t + \gamma_T dx_t - \alpha_T dz_t}{dz_t (1 - \beta_T x'_t + \alpha_T y'_t)} \simeq y'_t + \gamma_T x'_t - \alpha_T. \end{aligned} \quad (13)$$

There are six potential unknowns per tracker. Some simplifications can be made to lower the amount of unknowns. The  $z_T$  coordinate of each tracker is known to great accuracy from the survey. It may also be shown that the roll of the trackers has negligible influence on the alignment and may be ignored [19]. The beam-based detector alignment is critical to find the  $(x_T, y_T, \alpha_T, \beta_T)$  constants for each tracker.

590 The location of the TOFs is used as the reference for the tracker alignment. The line that joins the centre of TOF1 with the centre of TOF2 is chosen to be the reference axis. A deviation from this axis is considered as a misalignment of the trackers. Multiple scattering in the beam line does not allow to do the alignment on single particle basis but works for a larger sample of particles. The mean residual angles and positions of the trackers with respect to the TOF12 axis are an essential and powerful tool to infer the correction factors. Figure 49 shows the path of a single particle that scatters in the absorber module of the MICE experiment.

595 Each TOF provides a single space point in the global coordinate system  $(\xi_i, v_i, \zeta_i)$  with  $i$  the ID of the TOF. This position is assumed to be the true position with a large uncertainty due to the limited granularity of the detector ( $\sigma_x \sim \sigma_y \sim 17$  mm). The gradients of the track between the two TOFs are reconstructed as:

$$\psi'_{12} = \frac{\psi_2 - \psi_1}{\zeta_2 - \zeta_1}, \quad \psi = \xi, v. \quad (14)$$

The extrapolated position of the TOF reference track in the centre of tracker  $t = u, d$  is

$$\psi_{12}^t = \psi_1 + \frac{\psi_2 - \psi_1}{\zeta_2 - \zeta_1}(\zeta_T - \zeta_1) = (1 - \chi_T)\psi_1 + \chi_T\psi_2, \quad \psi = \xi, v, \quad (15)$$

with  $\chi_T = (\zeta_T - \zeta_1)/(\zeta_2 - \zeta_1)$ , the fractional distance from TOF1 to the tracker centre.

Tracker  $t = u, d$  samples the particle track in five different stations  $(x_t^j, y_t^j, z_t^j)$ , with  $j = 1, \dots, 5$ . This allows for the reconstruction of a straight track with gradients  $x'_t$  (resp.  $y'_t$ ) in the  $xz$  (resp.  $yz$ ) projection and its position at the centre,  $(x_t, y_t, 0)$ . No assumption is made on the prior position of the tracker and hence the coordinates and gradients are returned in local coordinates, i.e. assuming a tracker perfectly aligned with the beam axis, whose centre lies at  $z = 0$ .

In global coordinates, on average, the track reconstructed between TOF1 and TOF2 should agree with the track reconstructed in either tracker, i.e. the mean residuals should be zero. Applying this reasoning to the unknown offset and angles yields the following system of four equations with four unknowns [19]:

$$\begin{cases} \langle x'_t - \xi'_{12} \rangle = -\beta_T \\ \langle y'_t - v'_{12} \rangle = \alpha_T \\ \langle x_t - \xi_{12}^t \rangle = -x_T \\ \langle y_t - v_{12}^t \rangle = -y_T \end{cases}. \quad (16)$$

The measurement of four residual distributions per tracker yields the alignment constants.

The method described here assumes that the mean residuals can be measured with great accuracy and, more importantly, are unbiased. A bias in one of the residual distributions inevitably introduces a bias in the measurement of the corresponding alignment parameter, as they are directly proportional. The main source of bias is the scattering in the material between TOF1 and TOF2. If the beam is not perfectly centred, particles preferentially scrape out on one side of the magnet bore, anisotropically curbing a specific tail of the residual distribution. To nullify this effect, a fiducial cut is applied to the upstream sample. Only particles that are expected to be contained in the downstream tracker are included in the analysis [19].

### 9.3 Alignment of a data sample

Data is recorded with the superconducting magnetic channel of the experiment turned off, i.e. with tracks going in a straight line from TOF1 to the beam dump. High momentum beams are used in order to reduce the RMS scattering angle and maximize transmission. The settings used correspond to ‘pion’ beams of positive polarity to maximize statistics. The beams exhibit a variety of distributions in the beam line. An agreement between the independent fits guarantees an unbiased measurement of the alignment constants.

Provided with the unbiased sample produced as described in section 9.2, each track yields a set of global gradients between TOF1 and TOF2,  $\xi'_{12}$  and  $v'_{12}$ , and global extrapolated positions at the tracker centres,  $\xi_{12}^t$  and  $v_{12}^t$ . It also records the position of the track at the centre of the trackers in local coordinates,  $x_t$  and  $y_t$ , and its local gradients,  $x'_t$  and  $y'_t$ . The residual distributions necessary to measure the left hand side of equations 16 are produced in order to measure the eight alignment parameters. Figure 50 shows the gradient residuals between  $y'_u$  and  $v'_{12}$  for run 9367. The mean residual yields the the pitch of the upstream tracker,  $\alpha_U$ .

To ensure the best possible fit to the tracker parameters, the algorithm is applied multiple times. The first estimate of  $x_T, y_T, \alpha_T, \beta_T$  is used as an input to the sample selection part of the algorithm. The process is repeated until the alignment constants converge. Figure 51 shows the evolution of the optimal upstream tracker pitch,  $\alpha_U^*$ , over five iterations for run 9367.

Each data set was processed independently with the algorithm. Figure 52 compiles the alignment parameters measured for each run. The measurements are in good agreement with one another and show no significant

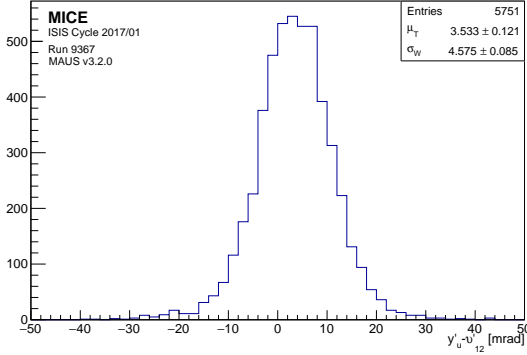


Figure 50: Residuals distribution between the pitch gradients measured locally in TKU,  $y'_u$ , and globally between TOF1 and TOF2,  $v'_{12}$ .

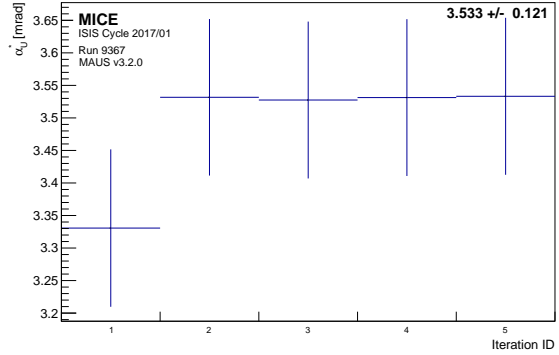


Figure 51: Evolution of the optimal value of the pitch angle in TKU,  $\alpha_U^*$ , for different number of iterations of the fitting algorithm.

discrepancy. The constant fit  $\chi^2/\text{ndf}$  is close to unity for each fit, which indicates that there are no significant additional source of uncertainty. The optimal parameters are summarised in table 12.

	x [mm]	y [mm]	$\alpha$ [mrad]	$\beta$ [mrad]
TKU	$-0.032 \pm 0.094$	$-1.538 \pm 0.095$	$3.382 \pm 0.030$	$0.412 \pm 0.029$
TKD	$-2.958 \pm 0.095$	$2.921 \pm 0.096$	$-0.036 \pm 0.030$	$1.333 \pm 0.030$

Table 12: Summary table of the optimal alignment constants measured in the high-momentum straight-track data acquired during the 2017/01 ISIS user cycle.

## 630 9.4 Propagation

The fitted parameters are used to yield the global track coordinates at the tracker  $t = u, d$  centres,  $(\xi_t, v_t, \zeta_t)$ , through equation 12 and the global gradients  $\xi'_t, v'_t$  through equation 13. A corrected global track is propagated in an adjacent detector module  $M$  at  $\zeta_m$  through

$$\psi_t^m = \psi_t + \psi'_t(\zeta_m - \zeta_t), \psi = \xi, v. \quad (17)$$

Provided exact corrections, a detector module  $M$  that measures a global position  $(\xi_m, v_m, \zeta_m)$  verifies

$$\begin{cases} \langle \psi_m - \psi_t^m \rangle = 0 \\ \langle \psi'_m - \psi'_t \rangle = 0 \end{cases}, \psi = \xi, v. \quad (18)$$

As a consistency check, the tracks are first propagated between the two trackers. The results are shown in figure 53. The top left and right distributions show the residuals between the TKU and TKD tracks at the centre of the downstream tracker and at the level of the absorber, respectively. The bottom two histograms show the agreement between the angles measured upstream and downstream. The azimuthal angle residuals show consistency between the roll of the two trackers.

The upstream tracker tracks are extrapolated into TOF1 and the downstream tracker tracks are propagated into the three downstream particle identification detectors: TOF2, the KL and the EMR. The residual plots are represented in figure 54. The values obtained show good agreement between the tracks and the space points measured in other MICE detectors.

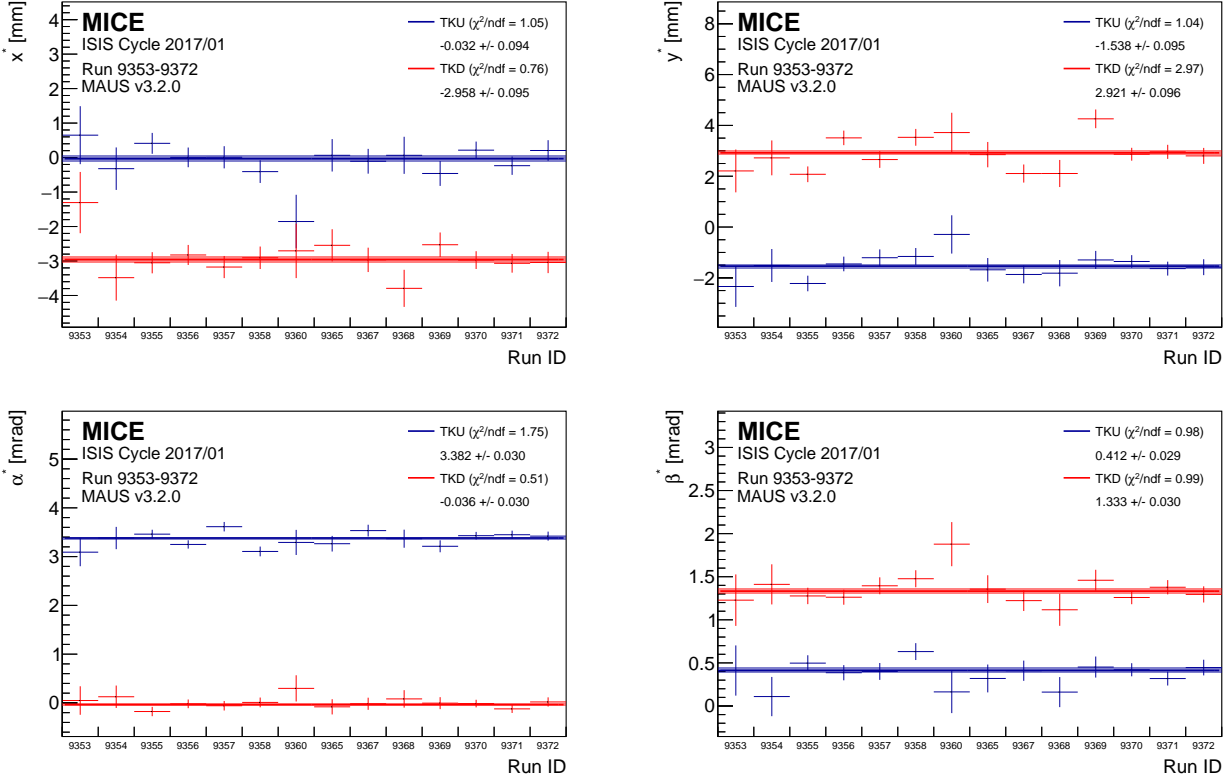


Figure 52: Consistency of the alignment algorithm across runs acquired during the 2017/01 ISIS user cycle.

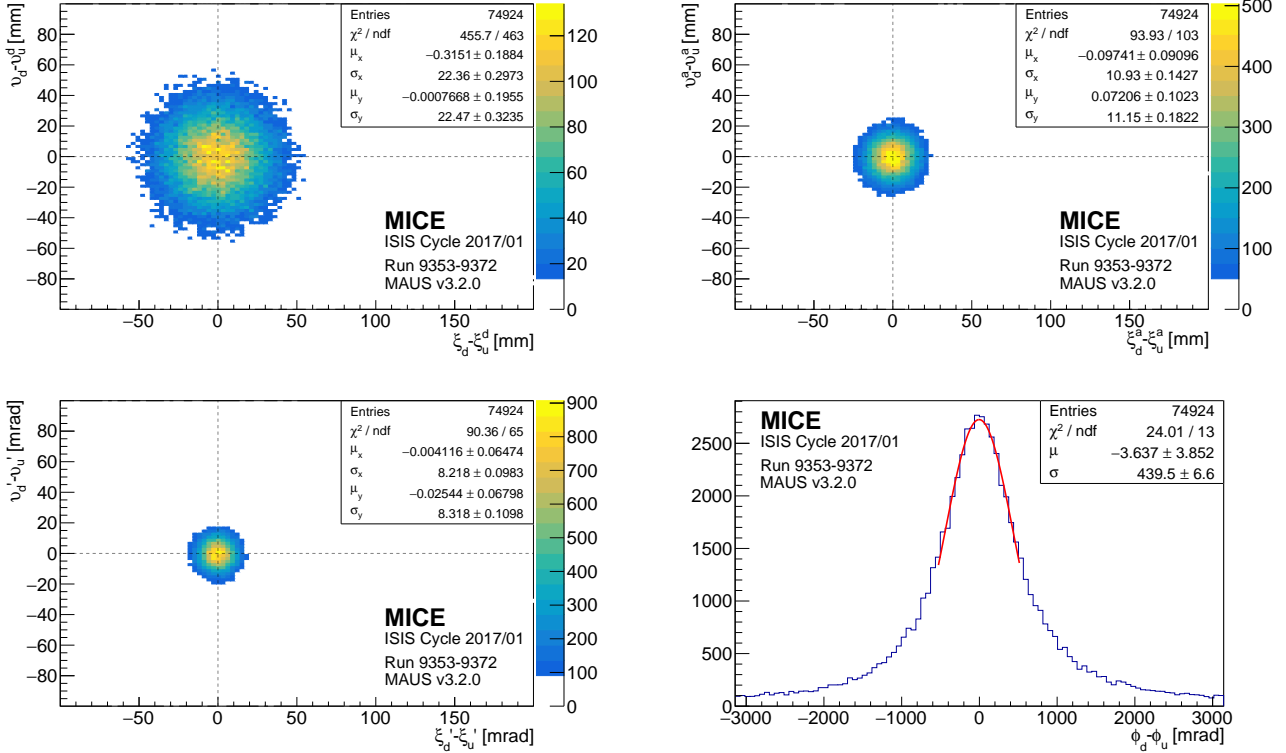


Figure 53: Tracker-to-tracker residual distributions in position (top) and angle (bottom).

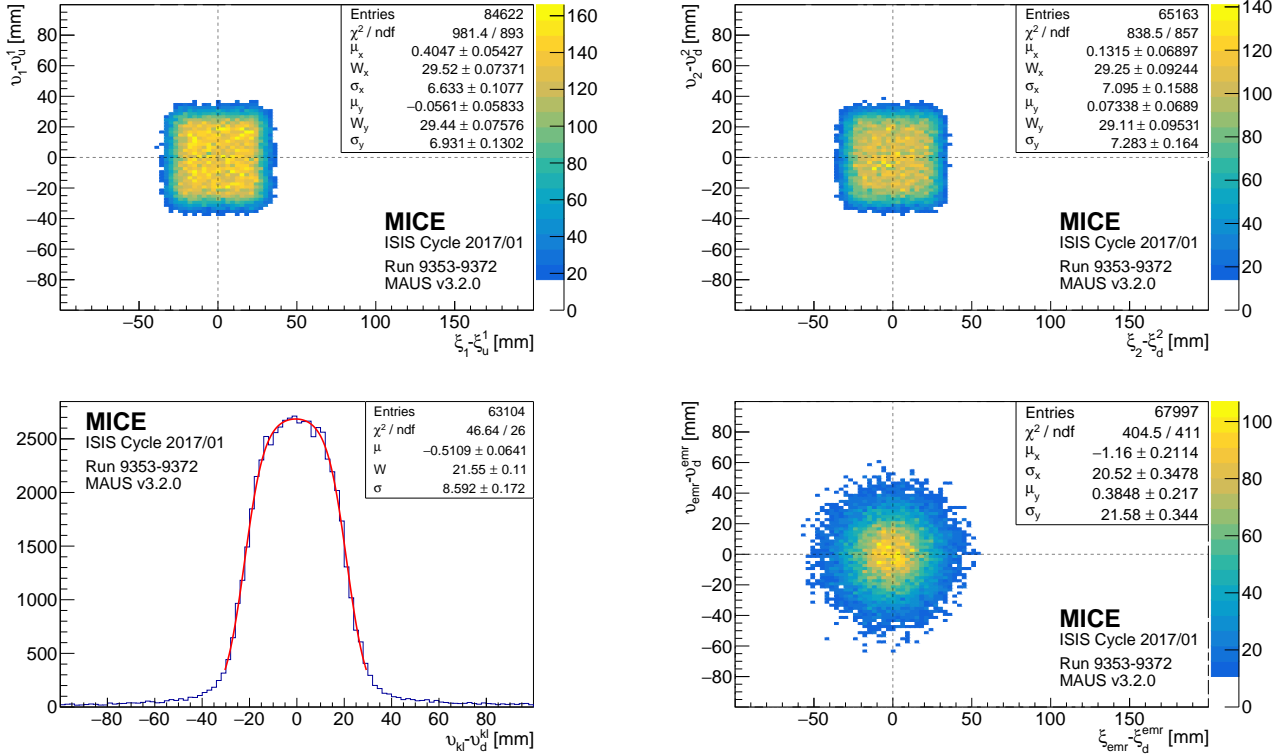


Figure 54: Tracker to particle identification detectors residual distributions (TOF1, TOF2, KL and EMR).

Special care is taken when evaluating the central value of the residual distributions. The two trackers and the Electron-Muon Ranger have a sufficient spacial resolution to follow a near-Gaussian distribution. The residuals involving these detectors are fitted with a standard multivariate normal of mean  $\mu$  and width  $\sigma$  between the two half-maximum, i.e. in the range  $\mu \pm 1.1775\sigma$ . The TOF hodoscopes and the KL do not have a sufficient resolution to produce residuals that follow a Gaussian distribution. A probability density function of the form

$$h(x) = \frac{1}{4W} \left( \tanh \left[ \frac{x - \mu + W}{\sigma} \right] - \tanh \left[ \frac{x - \mu - W}{\sigma} \right] \right) \quad (19)$$

is used in each projection to fit the residuals involving the low granularity detectors. The constant  $\mu$  represents the central value of the residual distribution,  $\sigma$  the residual width and  $W$  the half-width of one of the low-resolution detector pixel. The parameters obtained for each of the fits are represented on the residual graphs. The values found for  $W$  are consistent with pixels of 6 cm in TOF1 and TOF2 and of 4.4 cm in the KL.

## 10 Liquid Hydrogen absorber

### 10.1 Introduction

As a muon beam passes through material, some of the kinetic energy of the muons is lost through ionization of the material. This process results in a reduction of the normalised transverse emittance and the beam is said to be cooled. Muons will also undergo multiple Coulomb scattering which increases the divergence of the beam, thereby increasing the normalised transverse emittance and heating the beam.

The absorber vessel comprised a cylindrical aluminium body sealed with two thin aluminium end windows, as shown in the right panel of figure 55. The absorber vessel was specified to contain 22 l of liquid, so the body

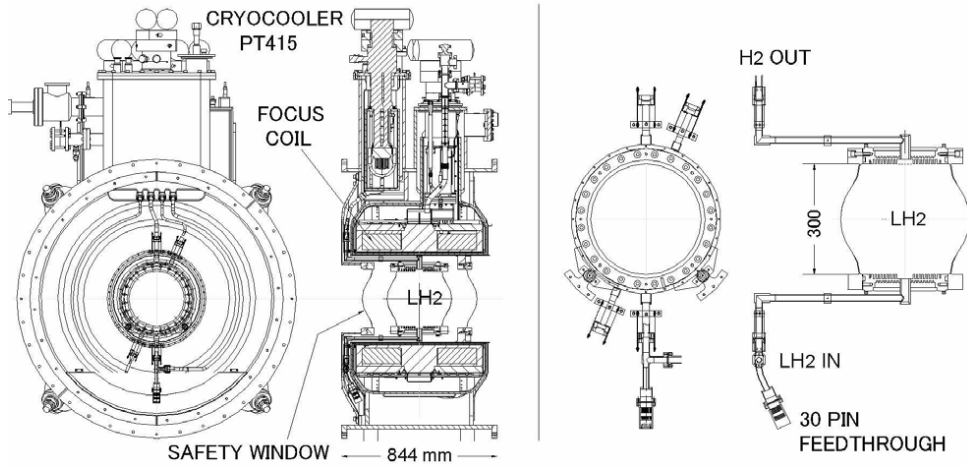


Figure 55: Left panel: Drawing of the absorber/focus-coil (AFC) module showing the principal components. Right panel: detail of the liquid-hydrogen absorber vessel.

had an inner diameter of 300 mm and a length between its end flanges of 230 mm. The length along the central axis between the two domes of the thin aluminium end windows was 350 mm. A detailed description of the construction of the absorber vessel is given in [20].

655 The following sections detail the important effects that could contribute to the systematic error of the measured energy loss and scattering in the absorber and thus the cooling effect.

## 10.2 Systematic studies

### 10.2.1 Variation of the density of liquid Hydrogen due to varying temperature and pressure

The energy lost by a muon travelling through the liquid Hydrogen absorber depends on the path length the  
660 muon travelled through and on the density of the liquid Hydrogen. The density of liquid Hydrogen changes at different temperatures and pressures. To know how much energy the muon lost, we need to accurately know the temperature and pressure to determine the density.

665 The temperature was recorded by eight LakeShore Cernox 1050 SD sensors. Four of the sensors were used solely as temperature sensors, while the other four were used as both temperature and level sensors. The level sensors were used when the absorber vessel was being filled to know how much liquid Hydrogen was in the vessel and during the experiment to ensure the liquid Hydrogen reached the top of the vessel.

670 They were arranged in pairs with two mechanically clamped at the top of the vessel, two at a rotation of 45°, a further two at a further rotation of 90° and a final two at a further rotation of 45° to be at the bottom of the vessel. The temperature sensors were labelled TSA, TSB, TSD and TSE from top to bottom, while the level sensors were labelled LSA, LSB, LSD and LSE from top to bottom.

675 cooldown and liquefaction were completed slowly over eight days until the 25 September 2017 at a pressure of 1.15 Bar after which the vessel's pressure was lowered to 1.085 Bar and stabilised during the early hours of the 26 September 2017 [20]. The vessel then remained in this steady-state equilibrium until the 16 October 2017 when the venting process began. During this process the coldhead was switched off and the heaters were switched on, delivering a nominal power of 50 Watt to the absorber vessel. This resulted in an increase in pressure and temperature until it stabilised at the boiling temperature. At this temperature the liquid Hydrogen turned to gas and began emptying from the vessel. A rapid increase in temperature followed once all the liquid

Table 13: The focus coil current correction coefficients calculated by plotting the temperature against current as the magnets are ramped up and down for each mode, straight and flip. The accuracy of the coefficients is limited by 0.1K resolution

Mode	LSA	LSB	LSD	LSE	TSA	TSB	TSD	TSE
Solenoid	3.9424E-4	4.6810E-4	1.2207E-3	5.7725E-5	7.1284E-5	2.8417E-4	4.2315E-4	3.7478E-4
Flip	5.5024E-4	-7.0037E-4	9.0778E-4	1.8262E-4	-4.2225E-4	-6.9633E-4	-2.0447E-4	6.2125E-4

Table 14: Temperature coefficient scaling factor for each sensor calculated by dividing the temperature reading (adjusted for cut-off coefficient and magnetic field) by the vaporisation temperature at that pressure

Mode	LSA	LSB	LSD	LSE	TSA	TSB	TSD	TSE
T/TBoiling	1.010581837	0.989245608	1.003371485	1.008424313	1.027755673	1.003697746	0.9784283	1.015526132

Hydrogen had boiled off.

The sensors have a typical accuracy of  $\pm 9\text{mK}$  and a long-term stability of  $\pm 12\text{mK}$  at 20K. The magnetic field dependent temperature error at 2.5T is 0.04%  $\Delta T/T$ , equivalent to  $\pm 8\text{mK}$  at 20K [21] [22]. These are the quoted uncertainties given by the manufacturer of the sensors. The importance of magnetic fields on temperature measurements is that they cause reversible calibration shifts. When the magnetic field is removed, the sensors return to their original calibration.

The Cernox 1050 SD sensors only recorded data to a resolution of 0.1 Kelvin for data storage considerations with any following decimal places cut-off and discarded. To be able to compare the temperature and pressure readings at a moment in time and to make the vast amount of data more manageable, a weighted mean was applied to the data [23]. To reduce the uncertainty in the liquid Hydrogen density a calibration procedure was devised using the boiling point (Eq. 20). The corrected temperature reading is found by applying a cut-off correction ( $c_{\text{cut-off}} = 0.05$ ), a magnetic field correction based on the focus coil current and mode, and then a boiling point scaling factor. The focus coil correction factors (Table 13) correspond to the slopes when current is plotted against temperature as the magnets are ramped up and down. The temperature coefficient in Eq. 20 is found by dividing the boiling temperature reading for that sensor by the boiling temperature of Parahydrogen at that pressure. In Eq. 20  $I$  is the focus coil current.

$$T_{\text{corrected}} = \frac{T_{\text{reading}} + c_{\text{cut-off}} - c_{\text{magnet}} I}{c_{\text{Temperature}}} \quad (20)$$

The Boiling temperature at 1.085 Bar is 20.511K, with our corrected sensor readings slightly higher (Fig. 56). There are however a number of uncertainties. Our readings are recorded to 0.1 K. The sensors add another 29mK (9mK accuracy + 12mK stability + 8mK magnetic field), although the magnetic field error is likely greater. The temperature scaling and magnet current correction factors also have an associated error as they are based on the 0.1K resolution. For example, a calibrated sensor at boiling temperature and 1.505 Bar should read 21.692K but can only read 21.65K (21.6K cut-off plus 0.05 cut-off correction) i.e. it is off by 0.042K. The pressure sensors have an uncertainty of  $\pm 5\text{mBar}$  which equates to  $\pm 0.016\text{K}$  during steady state. The pressure uncertainty ( $\pm 5\text{mBar}$ ) adds another uncertainty to the temperature calibration constants of  $\pm 0.014\text{K}$ . Collectively, all these uncertainties add up to 0.2K.

Knowing that in our steady state condition the liquid Hydrogen was close to the boiling temperature of liquid Parahydrogen [23] at  $20.5\text{K} \pm 0.2\text{K}$  and 1.085 Bar allows us to determine the uncertainty in the density as

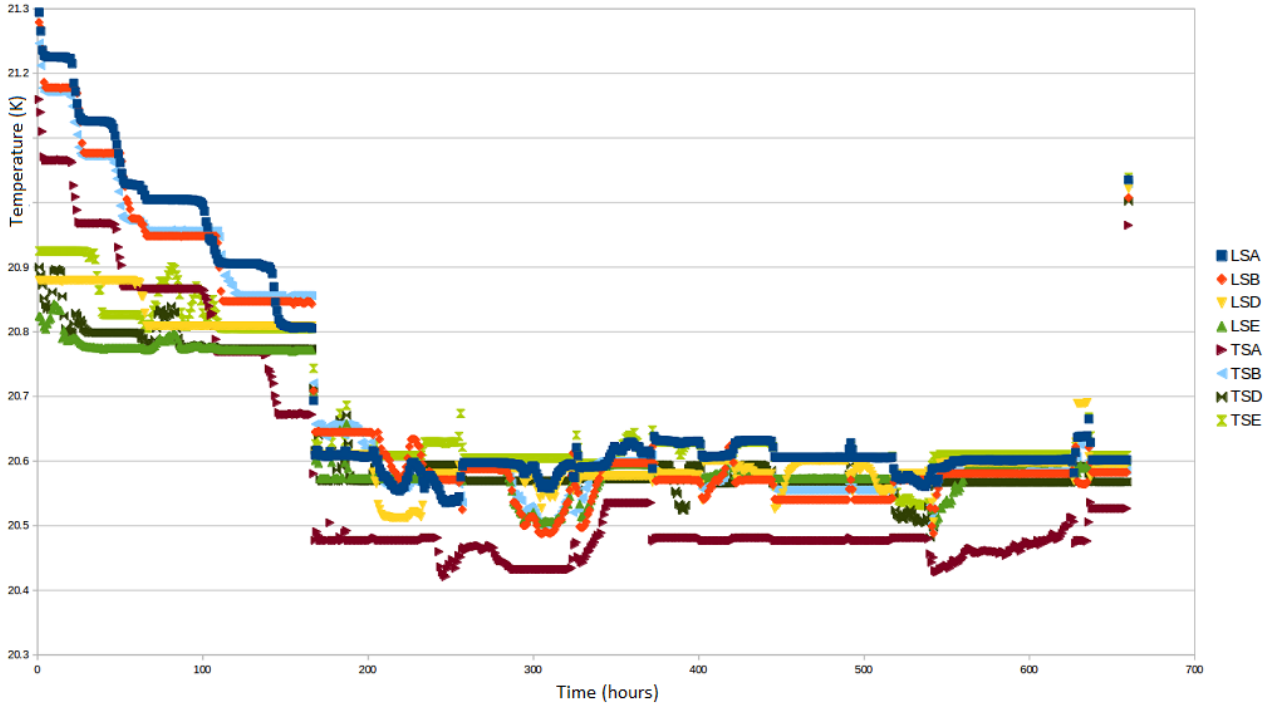


Figure 56: After applying all the correction factors the sensors agree to within 0.2K of each other during the steady state period. During the steady state period the boiling point temperature is 20.511K. Time is given as the number of hours since the 19 September 2017.

705  $70.54\text{kg/m}^3 \pm 0.24\text{kg/m}^3$

### 10.2.2 Contraction of the absorber vessel due to cooling

The Aluminium absorber vessel was cooled from room temperature to the operating temperature of the experiment ( $\approx 20.3\text{K}$ ), which resulted in the vessel contracting. The linear contraction of Al-6061 as it is cooled from  $293\text{K}$  is given by the equation

$$\alpha = -4.1277 \times 10^{-3}T - 3.0389 \times 10^{-6}T^2 + 8.7696 \times 10^{-8}T^3 - 9.9821 \times 10^{-11}T^4 \quad (21)$$

710 where  $T$  is the operating temperature [24]. The equation is a line of best fit of data collated by NIST (National Institute of Standards and Technology) and has an associated curve fit error of 4%.

At the MICE operating temperature, this corresponds to a linear contraction of the vessel along each plane of 0.415% ( $293\text{K} \rightarrow 20.3\text{K}$ ), resulting in a warm bore length (350mm) contraction of  $1.4525\text{mm} \pm 4\%$ . The vessel was held suspended in place, meaning the vessel was free to contract along each plane without restriction, 715 ensuring there were no forces created to distort the shape of the vessel.

### 10.2.3 Deflection of absorber vessel windows due to internal pressure

To minimise energy loss and Coulomb scattering by the absorber vessel, the windows were kept as thin as possible. They must however not rupture when handling any internal pressure they are subjected to. For safety considerations [20] [25] it is necessary for the liquid hydrogen circuit to be pressurised above atmospheric

720 pressure to prevent air ingress. The vessel must also be capable of handling up to 1.5 Bar, the relief valve set pressure.

These pressures resulted in a deflection of the absorber windows and were modelled by Green and Yang using ANSYS [26]. The uncertainty in the model's window deflection was 20%. It showed a linear expansion of the window deflection with pressure up to 2 Bar when the windows begin to yield.

725 The pressure sensors are accurate to  $\pm 5\text{mBar}$  (0.25% of 2 BarA Full Scale). At  $1085 \pm 5\text{ mBar}$ , the typical MICE operating pressure, this corresponds to a deflection of  $0.5374\text{mm} \pm 0.1076\text{mm}$  (model uncertainty)  $\pm 0.0022\text{mm}$  (sensor uncertainty) at the centre of the absorber window.

#### 10.2.4 Variation of the absorber vessel window thicknesses

730 The amount of energy loss and cooling experienced by a muon passing through the absorber depends on the amount of Aluminium and liquid Hydrogen traversed. There are four windows, two absorber wall windows of the vessel and two safety windows.

At the centre of the absorber, the total amount of Aluminium the muon beam passes through is  $785 \pm 24$  microns, a variance of 3.057%. However, as the windows are thin, the effects on energy loss are negligible. A 200MeV muon passing along the central axis of an empty absorber loses 0.345 MeV, which introduces a 0.01 MeV uncertainty on energy loss.

#### 10.2.5 Total Systematic Uncertainty on Energy Loss

In total there are three main contributions to the systematic uncertainty of the liquid Hydrogen absorber on energy loss. The contraction of the absorber and deflection of the absorber window due to internal pressure (Eq. 22) reduces the central warm bore length by  $0.4 \pm 0.3\text{mm}$ .

$$1.4525 (\pm 0.0581) - 2(0.5374 (\pm 0.1098)) = 0.3777 \pm 0.2777 = 0.4\text{mm} \pm 0.3\text{mm} \quad (22)$$

740 The combined absorber window thickness variation at the centre of the absorber is 24 microns. The temperature during the steady state period of the experiment when the pressure remained constant at  $1085 \pm 5\text{ mBar}$  is  $20.5 \pm 0.2\text{K}$  corresponding to a liquid Hydrogen density of  $70.54 \pm 0.24\text{kg/m}^3$ .

745 The energy loss is momentum dependent as each particle will lose a different amount of energy passing through the absorber. Tables 15 and 16 show the energy loss at various momenta and densities of Aluminium and liquid Hydrogen [27] [28] [29] [30]. 277 MeV and 344 MeV are the minimum ionization momenta of Aluminium and liquid Hydrogen respectively.

Table 15: Energy Loss for Aluminium (Al-6061) at various momenta with a density of  $2.699\text{ g/cm}^3$ .

Momentum (MeV)	100	140	200	277
Mass Stopping Power ( $\text{MeVg}^{-1}\text{cm}^2$ )	1.798	1.688	1.630	1.615
Stopping Power ( $\text{MeVcm}^{-1}$ )	4.8528	4.556	4.3994	4.3589

During the MICE experiment 140, 170, 200 and 240 MeV momenta muon beams were used. The energy loss and its uncertainty were then be calculated. The calculation used a central bore length of  $349.6 \pm 0.3\text{mm}$ , a total window thickness of  $0.785 \pm 0.024\text{mm}$  and a liquid Hydrogen density of  $70.54 \pm 0.24\text{kg/m}^3$  for a particle travelling straight through the centre of the absorber.

Table 16: Energy loss for liquid Hydrogen at various densities (0.0703 to 0.0708 g/cm<sup>3</sup>) and various momenta of muons.

Momentum	100	140	200	344
Mass Stopping Power	4.568	4.267	4.104	4.034
Stopping Power (at $\rho=0.0703$ )	0.3211	0.29997	0.2885	0.28359
Stopping Power (at $\rho=0.07054$ )	0.3222	0.30099	0.2895	0.2846
Stopping Power (at $\rho=0.07078$ )	0.3233	0.3020	0.29048	0.2855
Stopping Power (at $\rho=0.0708$ )	0.3234	0.3021	0.29056	0.2856

For a 140 MeV muon particle this corresponds to an energy loss of  $10.88 \pm 0.06 (\pm 0.51\%)$  MeV, while for a 200 MeV muon particle this corresponds to an energy loss of  $10.44 \pm 0.05 (\pm 0.51\%)$  MeV. In terms of Energy loss, the systematic error is 0.51%. This is for a particle travelling along the central axis of the absorber. An actual muon travelling through the absorber with a magnetic field will take a different path and thus have a different path length of Aluminium and liquid Hydrogen traversed.

755

### 10.3 Validation of the absorber model in MAUS

As a test of the absorber model, an analysis has been performed to measure the muon energy loss in the LiH and liquid Hydrogen absorbers and compare it to the energy loss predicted by the MC. A previous analysis measured this effect using only the TOF detectors [?] and found good agreement in the mean energy loss, but 760 did not have the precision to measure the shape of the distribution. In this updated energy loss analysis, the addition of the trackers allows better PID, slightly improved momentum measurements upstream compared to the TOF0-TOF1 measurement, and significantly improved momentum measurements downstream compared to the TOF1-TOF2 estimate.

Muons are selected using the particle ID described in Section 7. The muons' upstream momentum (before 765 the absorber) is measured using an average of the momentum measured by the tracker (at the plane nearest to the absorber) and the momentum calculated using the TOF0 to TOF1 flight time. This average is weighted by the expected resolution of the two measurements. (The resolutions are roughly the same for low-momentum muons, but the TOF measurement of momentum is less accurate for higher-momentum muons.) The muons' downstream momentum is measured solely using the downstream tracker.

The momentum change is measured for each beam momentum both with and without an absorber present. 770 The LiH ‘empty’ measurement is done with no absorber present, while the liquid Hydrogen ‘empty’ measurement is done with the hydrogen vessel in place, but not filled. The measurement with no absorber is used to find the resolution of the detector, and the measurement with a full absorber should then be a convolution of the true loss in the absorber and this resolution.

In order to extract the true momentum loss in the absorber, the ‘empty absorber’ result is modeled by a 775 gaussian distribution. The ‘full absorber’ measurement is then fit to a convolution of the true momentum loss (a landau distribution with free parameters) and the resolution of the detector (a gaussian distribution with parameters fixed by the ‘empty absorber’ fit).

The measurement of momentum loss is taken at four different beam momenta. It agrees well with the Monte 780 Carlo (in which the energy loss is modeled by GEANT) and with the predictions of the Bethe-Bloch formula, as shown in Figure 58.

- add LH2 plots

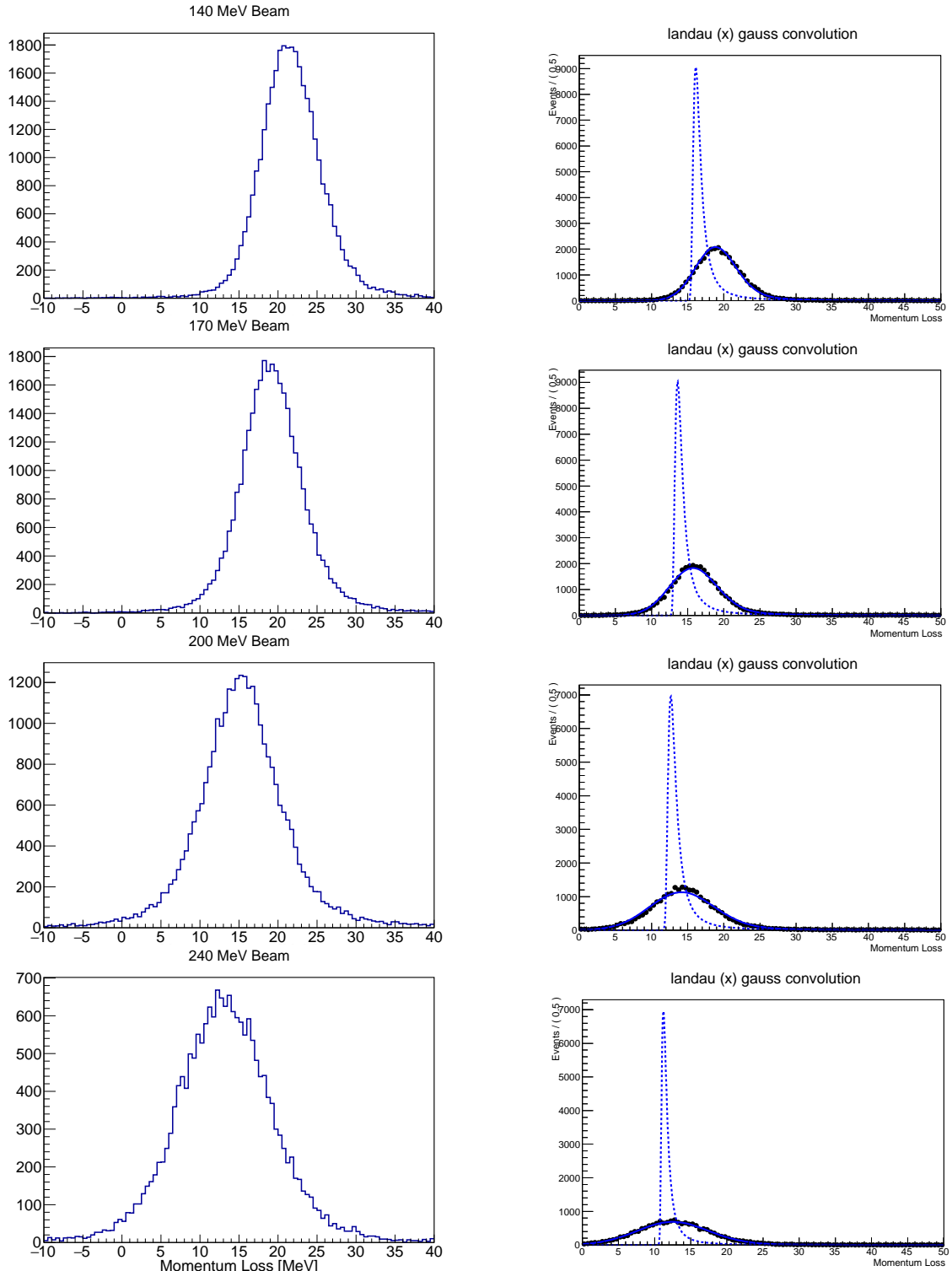


Figure 57: The measured momentum loss (left) and deconvolved distributions (right) in the MICE Lithium Hydride absorber. Four different momentum settings are shown: 140 MeV(a), 170 MeV(b), 200 MeV(c), and 240 MeV(d). The ‘deconvolved’ plots show the data (black points), the fitted convolved landau and gaussian (solid blue line) and the landau by itself (dotted blue line).

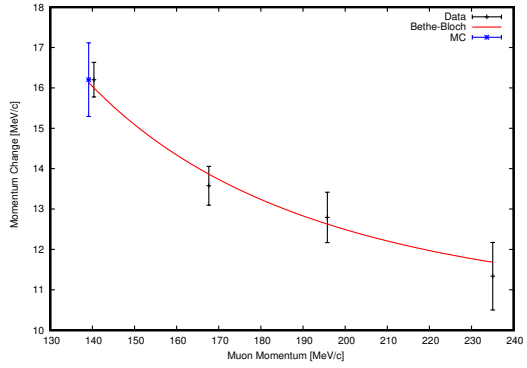


Figure 58: Comparison of measured momentum loss in data and in MC in Lithium Hydride. MPV of momentum loss is shown at each point with the prediction from the Bethe-Bloch formula shown as a solid line.

- systematics
- more words about comparing with MC and Bethe-Bloch

785 **11 Conclusions**

To be written at last.

## References

- [1] M. Bonesini, “The design of MICE TOF0 detector,” *MICE Note 145* (2006) .  
<http://mice.iit.edu/micenotes/public/pdf/MICE0145/MICE0145.pdf>.
- 790 [2] R. Bertoni *et al.*, “The construction and laboratory tests for MICE TOF0/1 detectors,” *MICE Note 241* (2008) . <http://mice.iit.edu/micenotes/public/pdf/MICE0241/MICE0241.pdf>.
- [3] R. Bertoni, A. Blondel, M. Bonesini, G. Cecchet, A. de Bari, J. S. Graulich, Y. Karadzhov, M. Rayner, I. Rusinov, R. Tsenev, S. Terzo, and V. Verguilov, “The design and commissioning of the MICE upstream time-of-flight system,” *Nuclear Instruments and Methods in Physics Research A* **615** (Mar., 2010) 14–26, arXiv:1001.4426 [physics.ins-det].
- 795 [4] R. Bertoni *et al.*, “The construction of the MICE TOF2 detector,” *MICE Note 286* (2010) .  
<http://mice.iit.edu/micenotes/public/pdf/MICE0286/MICE0286.pdf>.
- [5] D. Rajaram and V. C. Palladino, “The Status of MICE Step IV,”.  
<http://accelconf.web.cern.ch/AccelConf/IPAC2015/papers/thpf122.pdf>.
- 800 [6] M. Bonesini, “Progress of the MICE experiment,” arXiv:1510.08825 [physics.acc-ph].
- [7] The MICE Collaboration, “Characterisation of the muon beams for the Muon Ionisation Cooling Experiment,” *ArXiv e-prints* (June, 2013) , arXiv:1306.1509 [physics.acc-ph].
- [8] D. Adams *et al.*, “Pion contamination in the MICE muon beam,” *Journal of Instrumentation* **11** (Mar., 2016) P03001, arXiv:1511.00556 [physics.ins-det].
- 805 [9] M. A. Rayner, *The development of a novel technique for characterizing the MICE muon beam and demonstrating its suitability for a muon cooling measurement*. PhD thesis, Oxford U., 2011.  
<http://lss.fnal.gov/archive/other/thesis/rayner-m.pdf>.
- [10] Y. Karadzhov *et al.*, “TOF detectors Time Calibration,” *MICE Note 251* (2009) .  
<http://mice.iit.edu/micenotes/public/pdf/MICE0251/MICE0251.pdf>.
- 810 [11] L. Cremaldi *et al.*, “Progress on Cherenkov Reconstruction in MICE,” *MICE Note 473* (2015) .  
<http://mice.iit.edu/micenotes/public/pdf/MICE0473/MICE0473.pdf>.
- [12] R. Asfandiyarov *et al.*, “The design and construction of the MICE Electron-Muon Ranger,” *Journal of Instrumentation* **11** (Oct., 2016) T10007, arXiv:1607.04955 [physics.ins-det].
- 815 [13] F. Drielsma, “Electron-Muon Ranger: hardware characterization,” Master’s thesis, University of Geneva, 2014. <https://arxiv.org/abs/1710.06946>.
- [14] D. Adams *et al.*, “Electron-muon ranger: performance in the MICE muon beam,” *Journal of Instrumentation* **10** (Dec., 2015) P12012, arXiv:1510.08306 [physics.ins-det].
- [15] F. Drielsma, *Measurement of the Increase in Phase Space Density of a Muon Beam through Ionization Cooling*. PhD thesis, University of Geneva, 10, 2018.
- 820 [16] M. Ellis *et al.*, “The Design, construction and performance of the MICE scintillating fibre trackers,” *Nucl. Instrum. Meth.* **A659** (2011) 136–153, 1005.3491.
- [17] **D0** Collaboration, V. M. Abazov *et al.*, “The Upgraded D0 detector,” *Nucl. Instrum. Meth.* **A565** (2006) 463–537, physics/0507191.

- [18] Blot, S. and others, “Proton contamination studies in the MICE muon beam line,”.  
825       [accelconf.web.cern.ch/accelconf/ipac2011/papers/mopz034.pdf](http://accelconf.web.cern.ch/accelconf/ipac2011/papers/mopz034.pdf).
- [19] F. Drielsma, “Beam-based detector alignment in the MICE muon beam line,” arXiv:1805.06623  
[physics.ins-det]. <https://arxiv.org/abs/1805.06623>.
- [20] V. Bayliss *et al.*, “The liquid-hydrogen absorber for mice,” *Journal of Instrumentation* **13** no. 09, (2018)  
T09008. <http://stacks.iop.org/1748-0221/13/i=09/a=T09008>.
- 830 [21] “Cernox RTDs [Accessed 2 Oct. 2018],”.  
[https://www.lakeshore.com/Documents/LSTC\\_Cernox\\_1.pdf](https://www.lakeshore.com/Documents/LSTC_Cernox_1.pdf).
- [22] “Temperature Measurement and Control Catalog [Accessed 2 Oct. 2018],”.  
[https://www.lakeshore.com/Documents/LakeShoreTC\\_1.pdf](https://www.lakeshore.com/Documents/LakeShoreTC_1.pdf).
- [23] C. Brown *et al.*, “Systematic Uncertainties in the IH2 absorber,” *MICE Note 524* (2018) .  
835       <http://mice.iit.edu/micenotes/public/pdf/MICE0524/MICE0524.pdf>.
- [24] G. Hardin, “Aluminum 6061-T6 (UNS AA96061) [Accessed 3 Oct. 2018],”.  
<https://www.nist.gov/mml/acmd/aluminum-6061-t6-uns-aa96061>.
- [25] S. Ishimoto *et al.*, “Liquid Hydrogen Absorber for MICE,” *Conf. Proc. C100523* (2010) 421–423.
- [26] M. Green *et al.*, “Does One Know the Properties of a MICE Solid or Liquid Absorber to Better than 0.3  
840       Percent?,” *MICE Note 155* (2006) .  
<http://mice.iit.edu/micenotes/public/pdf/MICE0155/MICE0155.pdf>.
- [27] “Atomic and nuclear properties of Aluminium,”.  
[http://pdg.lbl.gov/2017/AtomicNuclearProperties/HTML/aluminum\\_Al.html](http://pdg.lbl.gov/2017/AtomicNuclearProperties/HTML/aluminum_Al.html).
- [28] “Atomic and nuclear properties of liquid Hydrogen,”. http:  
845       [http://pdg.lbl.gov/2017/AtomicNuclearProperties/HTML/liquid\\_hydrogen.html](http://pdg.lbl.gov/2017/AtomicNuclearProperties/HTML/liquid_hydrogen.html).
- [29] “Muon in Aluminium,”. http:  
[http://pdg.lbl.gov/2017/AtomicNuclearProperties/MUE/muE\\_aluminum\\_Al.pdf](http://pdg.lbl.gov/2017/AtomicNuclearProperties/MUE/muE_aluminum_Al.pdf).
- [30] “Muons in liquid Hydrogen,”. http://pdg.lbl.gov/2017/AtomicNuclearProperties/  
MUE/muE\_liquid\_hydrogen.pdf.